Advanced Energy Materials

ADVANCED ENERGY MATERIALS
www.advenergymat.de

RESEARCH ARTICLE OPEN ACCESS

Sustainable Carbon Fibers Enable Stable Long-Term Lithium Metal Deposition for Prospective Zero-Excess Lithium Metal Batteries

Samantha L. S. Southern[1,2] | Jonathon Cottom[3,4] | Jana B. Fritzke[2,5] | Emma N. Antonio[1] | Zhenyu Guo[1] | Bhavini Patel[1] | Romain Tort[1,6] | Ifan E. L. Stephens[2,6] | Camilla Di Mino[7] | Clare P. Grey[2,5] | Rhodri Jervis[2,8] | Emilia Olsson[3,4] | Heather Au[1,2] | Maria-Magdalena Titirici[1,2,9]

[1]Department of Chemical Engineering, Imperial College London, London, UK | [2]The Faraday Institution, Quad One, Harwell Science and Innovation Campus, Didcot, UK | [3]Advanced Research Center for Nanolithography, Amsterdam, The Netherlands | [4]Institute for Theoretical Physics, University of Amsterdam, Amsterdam, The Netherlands | [5]Yusuf Hamied Department of Chemistry, University of Cambridge, Cambridge, UK | [6]Department of Materials, Imperial College London, London, UK | [7]Physical and Theoretical Chemistry Laboratory, Department of Chemistry, University of Oxford, Oxford | [8]Electrochemical Innovation Lab, Department of Chemical Engineering, University College London, London, UK | [9]Advanced Institute For Materials Research, Tohoku University, Sendai, Japan

Correspondence: Emilia Olsson (e.olsson@arcnl.nl) | Heather Au (h.au13@imperial.ac.uk) | Maria-Magdalena Titirici (m.titirici@imperial.ac.uk)

Received: 13 December 2025 | **Revised:** 27 February 2026 | **Accepted:** 14 March 2026

Keywords: zero-excess | lithium metal anodes | lithium metal batteries | electrospinning | carbon fiber current collectors | lithiophilic hosts

ABSTRACT

Three-dimensional current collectors have emerged as a promising strategy to promote uniform Li deposition and extend the cycle life of zero-excess lithium metal batteries. However, excessive Li loss in the first cycle due to solid electrolyte interphase (SEI) formation on the large surface area, combined with the use of dense or nonrenewable materials and complex, multistep fabrication processes, limits their practical implementation. In this work, a lightweight, lignin-derived carbon fiber (CF) current collector is presented. It is fabricated via a simple and sustainable electrospinning process, and after carbonization has abundant structural defects and nanoscale porosity. Surface defects promote the formation of a stable, inorganic-rich SEI, efficiently passivating the current collector, while pores of ~1.0–1.4 nm enable quasi-metallic Li clusters to form before plating, providing a conductive network and distributed nucleation sites that enhance Li plating/stripping reversibility and cycle life. This CF current collector exhibits a first-cycle active Li loss of only 4.8%–8.9% relative to the typical Li inventory of commercial lithium-ion battery cathodes and maintains a coulombic efficiency of 99.0% over 200 cycles, demonstrating excellent electrochemical performance.

1 | Introduction

Full electrification of the transport sector, from road vehicles to aviation, demands batteries with higher energy density to minimize weight, and reduced reliance on critical raw materials to ensure sustainable and secure battery production [1]. While lithium-ion batteries (LIBs) have driven much of the progress so far, their continued dominance risks straining natural resources and limiting uptake in weight-sensitive sectors [2].

Zero-excess lithium metal batteries (ZELMBs) offer a promising alternative by replacing the conventional graphite anode with a bare current collector onto which Li metal is directly plated during operation. This configuration eliminates inactive anode

material, boosting energy density by substituting the theoretical anode capacity of graphite (372 mA h g^{-1}) with that of Li metal (3860 mA h g^{-1}) [3, 4].

However, poor Li plating and stripping reversibility severely limits cycle life, even with optimized electrolytes and cycling protocols [5–10]. On commercial copper foil surfaces, Li deposits nonuniformly due to high nucleation barriers, local current hotspots, and inhomogeneities within the solid electrolyte interphase (SEI). This nonuniform deposition evolves into morphological instabilities, such as needle-like dendrites or mossy Li, which disrupt the SEI, promoting ongoing electrolyte decomposition and Li loss [11, 12]. In addition, these high-surface-area Li metal structures are mechanically fragile, easily losing electrical contact during stripping, and generating inactive metallic Li [13].

Three-dimensional (3D) current collectors can improve deposition uniformity by distributing charge over a larger surface area, reducing local current density peaks, and accommodating volume changes [14]. Cu mesh modified with lithiophilic elements such as gold [15] or carbon coatings [16] have been explored; however, Cu remains a suboptimal material due to its poor lithiophilicity, high density, and limitations in sustainable supply. This highlights the need for lighter, more sustainable and inherently lithiophilic alternatives [10, 17–19].

Carbon nanofibers (CFs) are attractive substitutes, combining high conductivity, low density, and widely available precursors [20–23]. Pristine CFs, however, lack intrinsic lithiophilicity and typically require modifications to improve lithium-ion binding, lower nucleation barriers, and guide deposition. Common strategies include incorporating metal nanoparticles [24–26], introducing porosity, or doping with heteroatoms [27, 28]. While these modifications enhance deposition uniformity, the large surface area of CF current collectors promotes extensive SEI formation, so many are pre-lithiated to pre-form the SEI and compensate for Li loss, limiting true zero-excess operation [26, 29, 30].

Recent studies highlight the critical role of the current collector in influencing SEI formation. Multi-vacancy defective carbon paper [31] and Zn–N electrospun CF incorporating Zn–N_x defects [32] were shown to promote thin, inorganic-rich, and stable SEI layers by modulating the Fermi level of the carbon surface. These carbon structures achieved excellent capacity retention in ZELMBs, demonstrating that engineering the collector to control SEI properties is key for reversible Li cycling under zero-excess conditions.

CFs are typically derived from polyacrylonitrile (PAN), a petrochemical precursor that requires the use of polar, aprotic, and often toxic solvents such as dimethylformamide (DMF) during synthesis [25–27, 30]. Beyond sustainability concerns, the intrinsic PAN-derived framework provides the basic fibrous structure, but functional properties such as pores or heteroatoms require additional processing steps or material additions. For instance, micro- and meso-porosity can be introduced by incorporating pore-forming agents such as $Fe(acac)_3$ into the electrospinning solution, while O heteroatoms are commonly introduced through post-treatments such as nitric acid oxidation [27].

Lignin, by contrast, is a renewable biopolymer, predominantly obtained as a by-product of the pulp and paper industry [33]. Rich in O-containing functional groups within aromatic networks [34, 35], lignin can be dissolved in nontoxic solvents such as aqueous sodium hydroxide to produce electrospun CFs. Upon carbonization, it forms O-rich, turbostratic carbon structures with abundant microporosity and defect sites [36]. These intrinsic features can be tuned to enhance lithiophilicity and regulate SEI formation, Li nucleation and growth behavior. Lignin-derived CFs therefore offer a lightweight, sustainable, and inherently functional platform for ZELMB current collectors.

In this work, we demonstrate that ultralight lignin-derived electrospun CFs can serve as functional freestanding current collectors for ZELMBs. Through a combination of electrochemical testing, Raman spectroscopy, small-angle X-ray scattering (SAXS), gas adsorption, X-ray photoelectron spectroscopy (XPS), and *operando* solid-state ^{7}Li nuclear magnetic resonance (ssNMR) spectroscopy, we identify the structural and chemical features underpinning battery performance. By tailoring pore size, defect content and surface chemistry, these CFs promote thin, inorganic-rich SEI formation and support reversible Li deposition, achieving ~99.0% coulombic efficiency (CE) over 200 cycles and symmetric cell lifetimes exceeding 3000 h. In zero-excess configurations without a pre-formed SEI, the discharge capacity normalized to total electrode mass exceeds the theoretical capacity of graphite on Cu foil by ~66% and remains elevated over ~70 cycles.

2 | Carbon Fiber Synthesis and Characterization

CFs were fabricated via electrospinning a solution of organosolv lignin (OSL) and polyethylene oxide (PEO) in aqueous NaOH into a polymer fiber mat, which was subsequently carbonized under a nitrogen atmosphere. The OSL used was derived from beech wood and exhibits typical characteristics of hardwood lignin [37], including a high syringyl unit content (Figure S1), and a relatively low molecular weight ((M_W/M_N) = 1650/970 g mol^{-1}). A small quantity of PEO was incorporated as a plasticizer to enable electrospinning without the need for lignin fractionation, thereby improving scalability and cost-efficiency. NaOH served a dual role, aiding lignin dissolution and acting as a chemical activation agent, to enhance the porosity. The role of NaOH in the activation process of lignin-derived CFs has been investigated in our previous work, where it was found that activation occurs via the formation and thermal decomposition of sodium carbonate particles [38]. Additional mechanisms are expected to influence the final porosity including the melting of Na_2CO_3 (~851°C) and Na_2O (~1132°C), heteroatom removal, and carbon layer rearrangement, all of which can drive pore growth, coalescence, collapse, or closure. After carbonization, the CFs were washed to remove residual salt, revealing the developed pore structure.

To explore how temperature-dependent transformations affect the carbon structure and to produce CFs with distinct properties for performance evaluation, we selected three carbonization temperatures: 700, 1000, and 1300°C. The resulting materials (CF700, CF1000, and CF1300) were characterized in terms of porosity, defects, and graphitic ordering (Figure 1A).

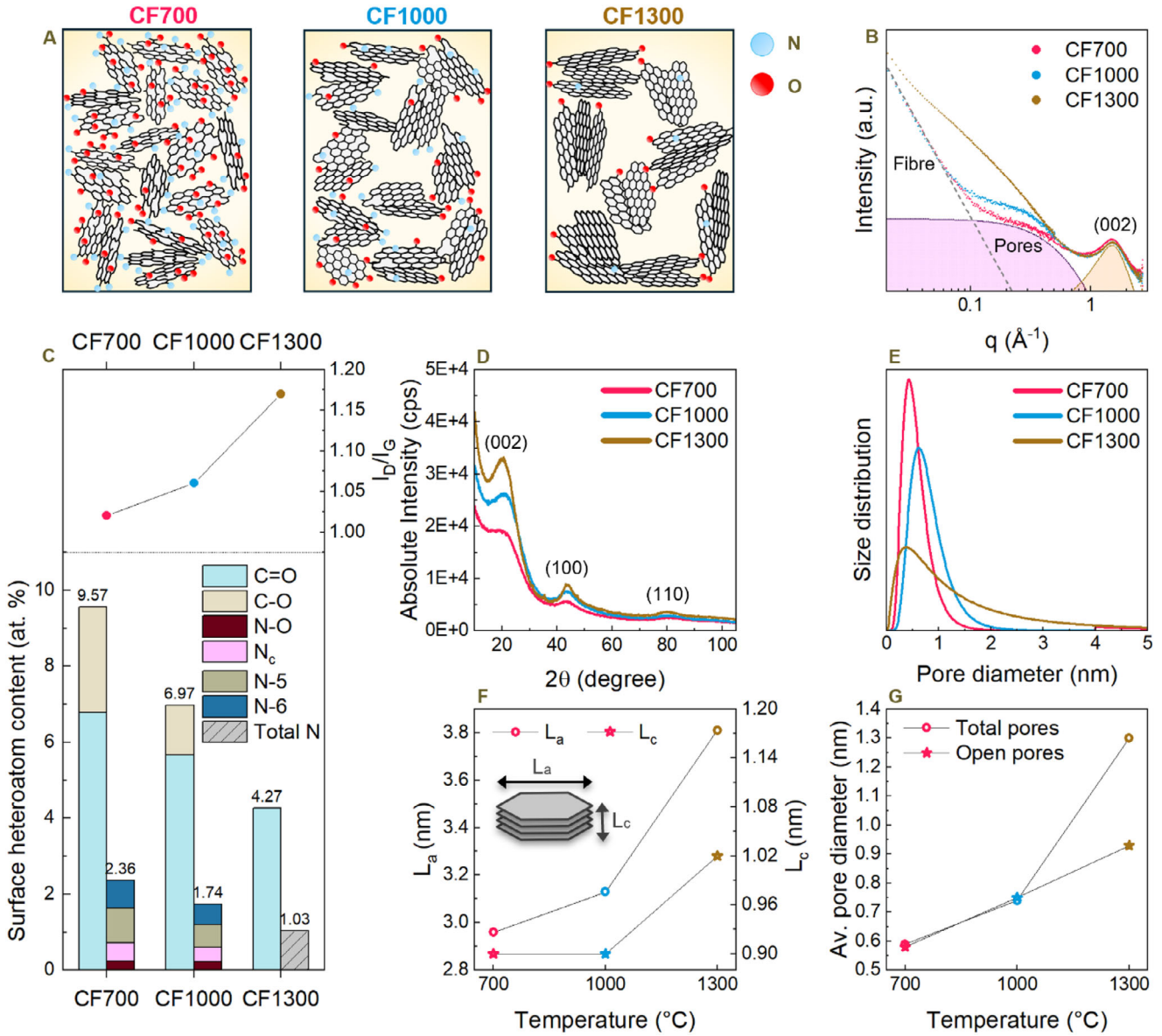

FIGURE 1 | Characterization of CFs carbonized at 700, 1000, and 1300°C. (A) Schematic diagram illustrating the structure of CF700, CF1000, and CF1300. (B) SAXS profiles for pristine fibers. (C) I_D/I_G peak ratio from fitting Raman spectra, and surface heteroatom content from XPS for pristine samples. CF1300: N 1s is too weak for component fitting; only total N shown. (D) XRD patterns for pristine fibers. (E) Pore size distributions obtained from modeling the shoulder region of the SAXS data for each pristine fiber material. (F) L_a and L_c values calculated from fitting XRD patterns for pristine fibers. (G) Average pore diameters from fitting SAXS profiles (see Supplementary Note 1 for fitting procedure), and average open pore diameters from fitting gas adsorption isotherms.

SAXS captures signals from both open and closed pores, providing a full picture of the pore architecture. Distinct SAXS profiles were observed for each pristine CF sample (Figure 1B), indicating clear structural evolution with temperature. Pore size distributions (Figure 1E) were obtained by fitting the shoulder region of the SAXS profiles (Table S1 and Figure S2). The mean pore diameter (Figure 1G) increased with carbonization temperature (0.59, 0.74, and 1.30 nm for CF700, CF1000, and CF1300, respectively), in line with trends observed in thermally activated hard carbon [39].

Open porosity was accessed via N_2 adsorption for micropores and mesopores (>~0.9 nm) and CO_2 adsorption for smaller micropores (<~0.9 nm). CF700 contained a high fraction of accessible ultra-micropores (<~0.5 nm), largely absent in CF1000 and CF1300, contributing to its high surface area of 642 m^2 g^{-1} (Table S2 and Figure S4). Adsorption data indicated a progressive increase in open pore size with carbonization temperature, consistent with SAXS measurements of overall pore size (Figure 1G). In CF1300, however, the average pore size from SAXS (1.30 nm), was substantially larger than that from gas adsorption (0.93 nm), suggesting the formation of large, closed pores inaccessible to adsorbates. These sealed pores reflect significant structural reorganization at 1300°C, likely driven by the onset of graphitization within the fiber interior.

Raman spectroscopy was used to assess structural disorder in the CFs. The broad D and G bands (Figure S5) arise from

the defect-activated breathing mode of aromatic rings and the relative motion of sp^2 carbon atoms, respectively. According to Ferrari's three-stage model, our CFs fall into stage two, where I_D/I_G scales with the graphitic cluster area (L_a^2) [40]. The calculated values of I_D/I_G (Figure 1C) derived from the fitted Raman spectra (Figure S5), therefore reflect a reduction in structural disorder and growth of larger graphitic domains with rising carbonization temperature, as expected. This increase in domain size was confirmed by XRD (Figure 1D), as indicated by changes in the (002) reflex, corresponding to the interlayer spacing between graphene sheets, and the (100) reflex, associated with in-plane atomic arrangement. The calculated crystallite dimensions, L_a (in-plane) and L_c (stacking height), both increase with carbonization temperature, confirming progressive graphitization (Figure 1F). The interlayer spacing (d_{002}) remained approximately constant at ~0.41 nm across all samples. The persistence of wide interlayer spacing despite overall increased structural order may result from the branched nature of the lignin precursor, which hinders tighter stacking of graphene layers [35].

The decreasing defect content with increasing carbonization temperature observed in the Raman spectra was corroborated by XPS analysis of surface heteroatom concentrations (Figure 1C, Figure S6 and Table S3), which showed an overall decline in O and N. Across all CFs, C═O groups were more abundant than C—O groups, consistent with the higher stability of the C═O bond. Four N configurations were identified: oxidized N (N—O), graphitic N (N_c), pyrrolic N (N-5), and pyridinic N (N-6).

To assess the energetic stability of O and N defects, density functional theory (DFT) simulations were performed following on from our previous work [41–45]. Hard carbons are turbostratic and structurally heterogeneous; an atomistically faithful model would necessarily couple defect chemistry with local curvature, pore topology/connectivity, and stacking disorder, making attribution of relative contributions challenging. We therefore use idealized planar and curved graphene/pore motifs in which defect types, interlayer spacing, and pore diameters are controlled to decouple these variables and extract trend-level relationships, rather than to reproduce the full carbon fiber microstructure. These simulations confirmed that the formation of both O- and N-containing defects is energetically favorable (Figure S7), with defects in curved nanopores being significantly more stable than those on basal planes or planar motifs [44]. In addition, a systematic relationship between pore diameter and defect formation energy was observed (Figure S8). For defects with a vacancy site (V_c), the formation energy gradually increases with pore diameter, reflecting the progressive reduction in local curvature-induced strain. Vacancy-type defects are strongly favored in small pores (diameter < 1.4 nm) to minimize strain in the carbon lattice. However, they become significantly less favorable in larger pores (diameter > 1.4 nm) because the defect can relax to form a C_5-ring, reducing the number of unsaturated bonds. In contrast, substitutional N defects exhibit nonmonotonic behavior: N_C formation is least favorable in highly confined pores (diameter <~1.0 nm), most favorable in pores around 1.4 nm, but then gradually becomes less favorable as pore size increases beyond this optimal diameter.

3 | Lithium Insertion and SEI Formation on Carbon Fibers

3.1 | First Cycle Electrochemistry

The initial charge–discharge cycle in ZELMBs is critical to battery lifetime and energy density, as a significant portion of active Li is consumed to form the SEI at the anode during this cycle. This Li loss is amplified when using 3D current collectors, which expose larger electrochemically active surface area to electrolyte. The composition, morphology, and thickness of the SEI formed during this first cycle also strongly influences subsequent Li plating and stripping behavior [46].

To investigate the electrochemical processes at the CF current collectors during this initial cycle, we assembled CF/Li half cells and conducted galvanostatic cycling with a voltage cutoff limit of 0 V vs Li^+/Li (hereafter referred to simply as V). The electrolyte was lithium bis(trifluoromethyl sulfonyl)imide (LiTFSI) dissolved in 1,3-dioxolane (DOL) and 1,2-dimethoxy ethane (DME) (1:1 by volume) with 5 wt% lithium nitrate ($LiNO_3$). This electrolyte combination is commonly employed in LMB research due to its electrochemical stability and its ability to facilitate formation of a favorable SEI. $LiNO_3$ acts as a sacrificial additive, undergoing reductive decomposition to generate inorganic species that enhance interfacial passivation, with its effectiveness dependent on the total additive inventory relative to the reactive Li surface area generated during cycling, while DOL contributes flexible polymeric components. Together, these electrolyte components enhance Li plating and stripping reversibility [47–50].

The discharge–charge profiles (Figure 2A) and corresponding differential capacity (dQ/dV) plots (Figure 2B) reveal multiple stages of electrolyte decomposition, highlighted by the shaded potential regions. According to previous studies, the reduction of nitrate (NO_3^-) typically begins at ~1.7–1.8 V vs Li^+/Li [51–54], aligning with the first prominent reduction peak observed across all our samples. We therefore attribute a contribution of these features to NO_3^- reduction. At lower potentials, additional peaks appear which are likely associated with the reduction of ether solvents (DOL/DME). However, precise assignment of these features remains challenging due to the complex and overlapping nature of electrolyte decomposition pathways, involving multiple concurrent reactions and intermediate species.

CF700 and CF1000 exhibit similar reduction peak potentials at ~1.7 and 1.3 V, suggesting comparable SEI formation pathways. In contrast, CF1300 shows a pronounced shift of the second irreversible feature to ~0.95 V, pointing to the formation of distinct SEI species. Moreover, CF1300 displays additional irreversible peaks below 0.25 V, contributing to a large total first-cycle capacity loss (Figure 2C). This continued SEI formation at low potentials suggests that the initial SEI formed at higher potentials is insufficiently passivating.

CF1000 exhibits the lowest first-cycle capacity loss (0.16 mA h cm^{-2}), nearly identical to that reported for multivacancy-defective carbon paper [31] specifically designed to tune SEI formation through engineered surface defects. First-cycle capacity loss values are rarely reported for electrospun hosts, as the

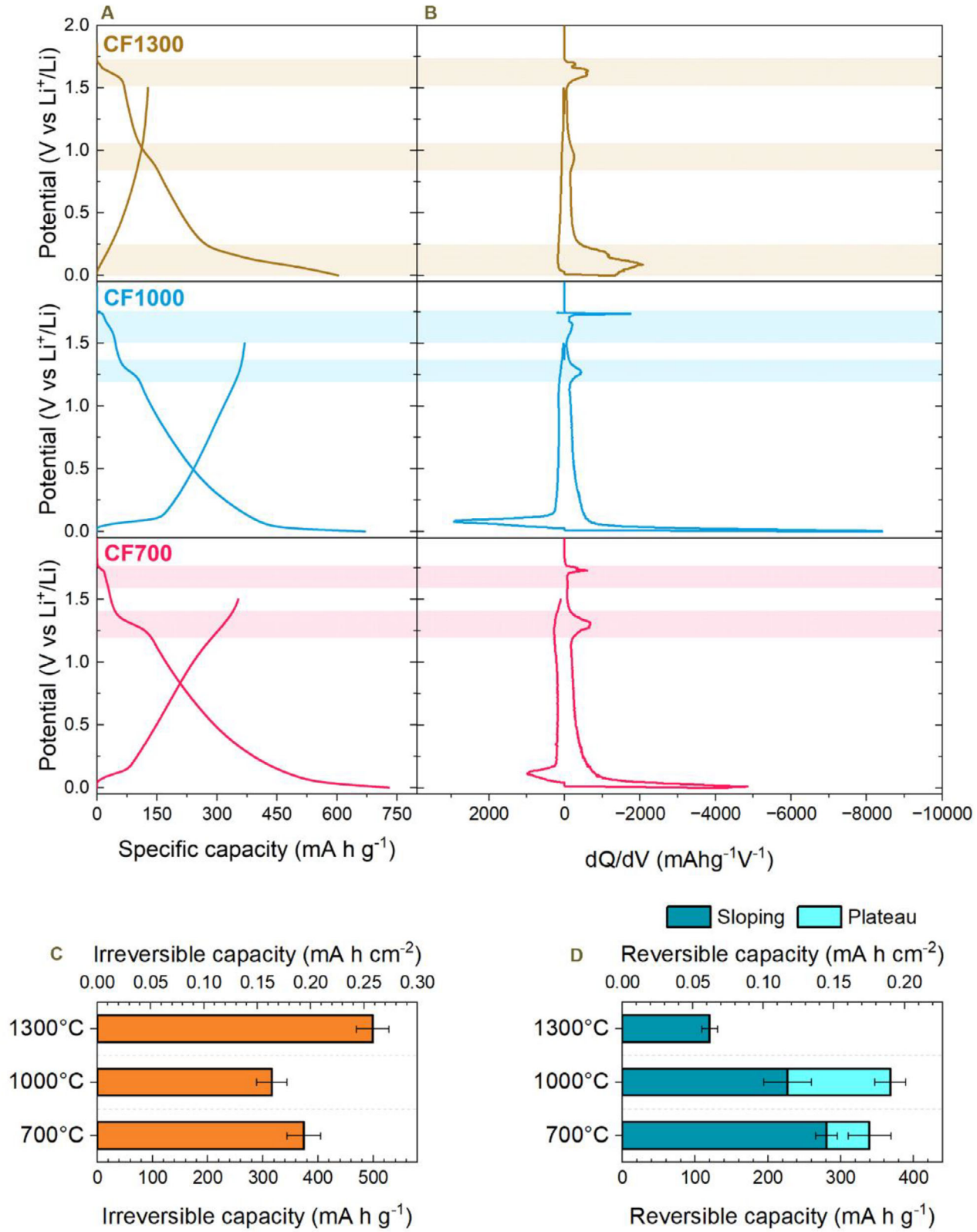

FIGURE 2 | Electrochemical characterization of the initial SEI formation cycle. (A) Potential–capacity profiles of the first discharge and charge cycle from 0 to 1.5 V for CF700, CF1000, and CF1300, cycled at 0.1 mA h cm^{-2}. (B) Corresponding dQ/dV plots, with shaded regions highlighting irreversible processes (capacity values are given with respect to the CF current collector). (C) Irreversible capacities extracted from the initial cycle. (D) Reversible capacities extracted from the initial cycle. For (C) and (D), capacities are normalized to both the CF mass and the geometric electrode area.

SEI is commonly pre-formed prior to full-cell assembly, such that the large initial irreversible Li consumption does not limit the performance [25, 26, 29, 32]. Commercial LIB cathodes typically deliver areal capacities of ~1.8–3.3 mA h cm^{-2} [3]. Thus, the observed loss represents only ~4.8–8.9% of the available Li inventory when paired with LIB cathodes in zero-excess configurations. For comparison, conventional LIBs typically consume 5–20% of the available Li inventory during initial SEI formation on graphite anodes [55]. Therefore, the irreversible Li loss observed here is well within the range of established commercial systems.

While these CF materials serve as Li metal current collectors rather than typical LIB anodes, they can still accommodate some Li-ion storage prior to metallic Li plating. In the voltage profiles, a reversible sloping region is observed, corresponding to Li^+ adsorption, and a reversible plateau region, associated with pore filling [56]. The reversible sloping capacity decreases with increasing carbonization temperature (Figure 2D), consistent with a reduction in defect content and thus available Li^+ adsorption sites. In contrast, the plateau capacity increases from 700 °C to 1000°C, suggesting enhanced pore-mediated clustering.

To assess the impact of the carbon morphology, a reference electrode was prepared from directly carbonized bulk lignin powder. In contrast to CF1000, the powder-derived electrode carbonized at 1000°C exhibits only sloping reversible capacity during the first discharge and shows no discernible low-potential plateau region (Figure S9), indicating that this storage behavior is enabled by the electrospun fiber architecture.

No plateau capacity is observed for the fibers carbonized at 1300°C, indicating that the pores at this temperature are no longer accessible for Li storage, possibly due to a pore environment that disfavors clustering and/or the formation of a Li^+ blocking SEI.

3.2 | SEI Characterization

To probe differences in SEI chemistry and structure between the three CF materials, we performed *ex situ* XPS at multiple etching depths. Samples were disassembled at 0.25 V and 0 V during the first discharge step to capture the chemical evolution of the SEI as it formed at the current collector.

The normalized content of different C 1s environments within the SEI layers at 0.25 V is shown in Figure 3A. The intensity of the C–Li peak at ~283 eV increases with etching depth, suggesting it originates from Li bonded to the underlying carbon current collector [57]. This contribution decreases with increasing carbonization temperature, consistent with the lower defect content, and therefore reduced surface reactivity toward Li [58].

Peaks in the 286–289 eV range (C—O, C═O, and $RCOO^-$) were assigned to O-containing organic species, likely formed from DOL or DME reduction, including lithium alkoxides (LiOR), lithium ethers (R-CH_2OLi), and lithium formate (HCO_2Li) [54, 59, 60]. The relative intensity of these peaks decreases with etching depth, in line with the bilayer SEI model proposed by Peled et al., where a compact inorganic layer lies adjacent to the electrode and a porous organic layer faces the electrolyte [46].

The C—C/C═C peak at 285.0 eV, observed at the outermost SEI surface without etching (Figure S10) contrasts with the predominantly sp^2 C peak at 284.5 eV in the underlying pristine CFs (Figure S6). The higher binding energy, together with the increased contribution from O-containing organic species, indicates that this feature originates from polymeric or oligomeric SEI species rather than from the intrinsic CF structure [61].

For CF700 and CF1000, the C—C/C═C peak dominates the carbon environments at the SEI surface and decreases with etching in parallel with the O-containing organic species. This co-evolution indicates that both signals originate from polymeric organic SEI components. In contrast, CF1300 exhibits a smaller C—C/C═C contribution relative to O-containing organic species, consistent with the formation of shorter-chain organic intermediates. With increasing etching depth, the O-containing organics peak diminishes while the C—C/C═C peak grows, indicating that the latter increasingly reflects the exposed CF substrate rather than SEI-derived organics. These observations suggest that the SEI formed on CF1300 at 0.25 V is less polymeric than the SEI on CF700 and CF1000.

The presence of polymeric species is consistent with DOL reduction chemistry [47, 48]. Upon reduction, DOL undergoes anionic ring-opening polymerization to form poly(DOL), while also generating intermediate products such as HCO_2Li and LiOR. The resulting polymeric layer imparts elasticity to the SEI, producing a film that is adherent and capable of accommodating electrode volume changes, which is critical for smooth Li deposition. On more reactive surfaces, such as CF700 and CF1000, anionic polymerization is likely favored, leading to a polymer-rich SEI at 0.25 V. On CF1300, where reactive surface sites and Li^+ adsorption are limited at 0.25 V, polymerization is hindered, and only shorter-chain intermediates accumulate.

Figure 3C presents the normalized lithium oxide (Li_2O) content, obtained from O 1s spectra, within the SEI at 0.25 V. Three distinct features were observed in the O 1s spectra (Figure S10): a low binding energy peak at ~528 eV, attributed to Li_2O, and two higher binding energy peaks corresponding to a mixture of lithium carbonate (Li_2CO_3), lithium hydroxide (LiOH), and organic species. The Li_2O fraction increases with etching depth, consistent with the proposed bilayer SEI structure [46]. Notably, while CF700 shows a stronger increase in Li_2O fraction with etching than CF1000, considerably less Li_2O is detected at the outer surface. In CF700, the inner inorganic layer may be buried beneath a thicker or more organic-rich outer layer, which obscures the Li_2O signal at the surface.

CF1300 exhibits a markedly lower Li_2O content at 0.25 V compared to CF700 and CF1000, which is noted alongside the absence of lithium nitride (Li_3N) at ~397 eV in the N 1s spectrum (Figure 3D). Li_2O is a stable SEI component with roughly twice the Li^+ conductivity of LiF, promoting homogeneous Li^+ flux [62]. Meanwhile, Li_3N, formed via the complete reduction of NO_3^- anions [51, 52, 54, 63], is among the most ionically conductive SEI species, enabling highly efficient Li^+ transport [62, 64]. In CF700 and CF1000, surface defects such as edge sites and vacancies may facilitate interfacial electron transfer and Li^+ adsorption, which are required for full NO_3^- reduction to Li_3N [65]. N-6 may further enhance these reactive sites by localizing electron

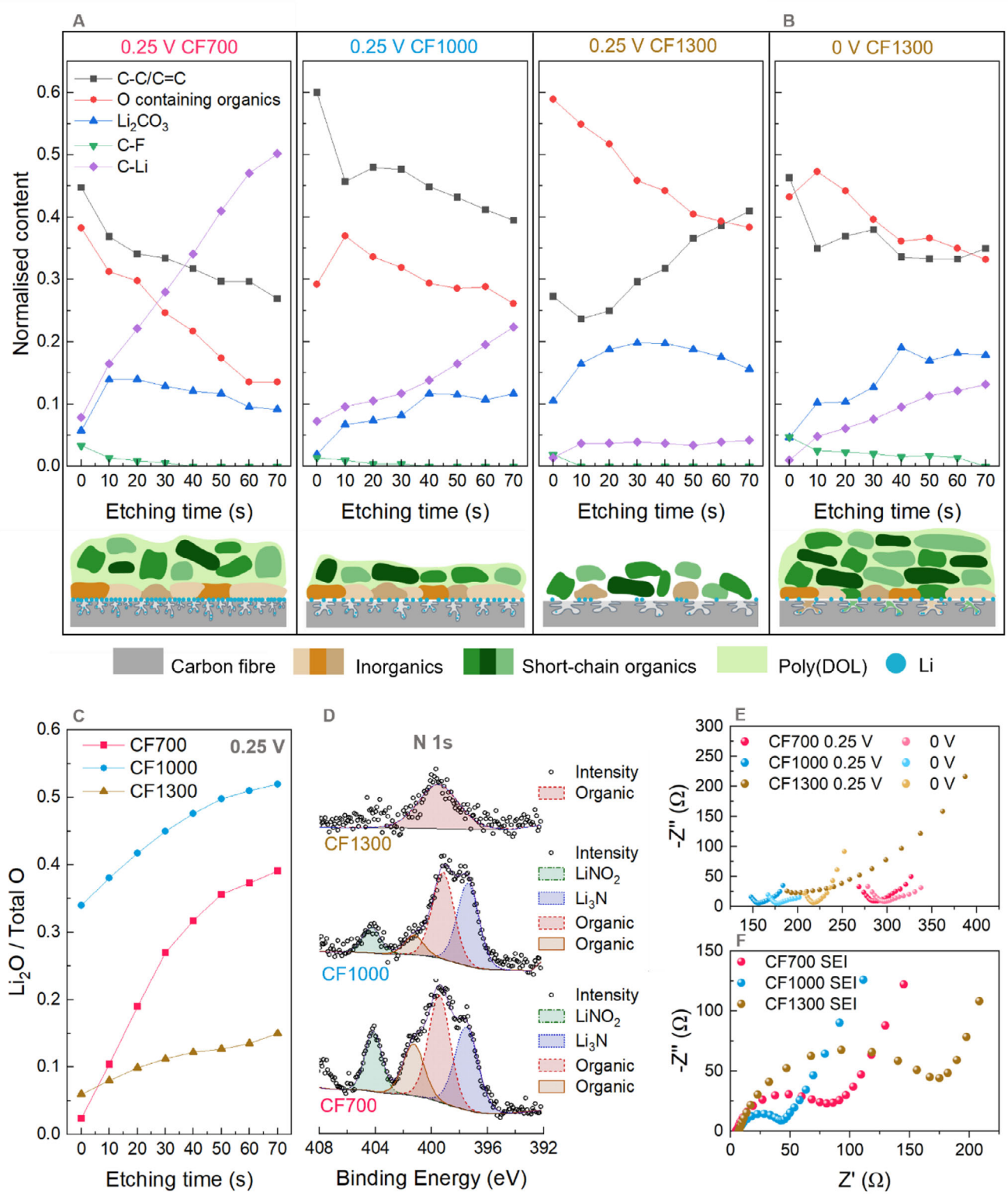

FIGURE 3 | XPS and EIS characterization of the initial SEI formation cycle. (A) The normalized C 1s peak contributions as a function of etching time for *ex situ* CF electrodes discharged to 0.25 V, and corresponding schematics illustrating the SEI structures. (B) The normalized C 1s peak contributions as a function of etching time for *ex situ* CF1300 electrode discharged to 0 V, and a corresponding schematic illustrating the SEI structure. (C) Li_2O/total O peak intensity vs etching time for *ex situ* CF electrodes discharged to 0.25 V. (D) N 1s fitted spectra for *ex situ* CF electrodes discharged to 0.25 V. (E) EIS of CF electrodes discharged to 0.25 and 0 V at frequencies 25–0.01 Hz. (F) EIS of samples at 1.5 V after three SEI formation cycles at frequencies 1 MHz to 0.1 Hz.

density at the carbon edge [66]. CF1300, however, has low defect content and lacks N-6 (Figure 1C), resulting in few reactive sites. Although N_c and N-5 are present, their electrons are delocalized or less accessible, making them less effective in promoting Li_3N formation.

Ex situ samples at 0 V were analyzed to examine SEI evolution below 0.25 V. For CF700 and CF1000, normalized peak contributions remained largely unchanged (Figure S11), indicating that the SEI formed above 0.25 V is stable and passivating, consistent with electrochemical data. In contrast, CF1300 shows significant spectral changes at 0 V (Figure 3B), including an increased C—C/C═C intensity at the SEI surface, suggesting the formation of polymeric organic compounds. To investigate the evolution of inorganic species, we performed titration experiments to quantify the main inorganic components of the SEI on CF1300 (Li_3N, LiF, and Li_2O/LiOH) at 0.25 V and 0 V (see Supplementary Note 4). The data (Table S4) show an increase in Li_3N and Li_2O/LiOH at 0 V compared to 0.25 V, resulting in an approximately twofold increase in total inorganic content, although the overall amount remains lower than that of CF700 and CF1000. Together, these results suggest that the SEI formed on CF1300 up to 0.25 V is insufficiently passivating, allowing continued SEI formation at lower potentials. Below 0.25 V, the stronger driving force for Li^+ adsorption and solvent reduction likely facilitates SEI growth, potentially extending into the larger open pores (>2 nm) of CF1300 [31, 65].

The continued SEI growth on CF1300 below 0.25 V can be attributed to two key factors. First, the SEI formed above 0.25 V contains only small amounts of inorganic species, which typically form dense, ionically conductive, and passivating films [31]. Instead, the SEI is dominated by short-chain, organic intermediates, which are expected to form more porous, permeable films that allow electrolyte molecules to continue reaching the electrode surface, sustaining electrolyte decomposition. Second, the reduced defect content and lower surface reactivity of CF1300 likely cause electrolyte reduction to occur at isolated, reactive sites rather than uniformly across the surface. This localization inhibits the formation of a continuous, robust SEI, enabling ongoing decomposition at low potentials.

To further investigate the processes occurring between 0.25 V and 0 V, we performed electrochemical impedance spectroscopy (EIS) in the low-frequency region (25–0.01 Hz), probing Li^+ diffusion and capacitive behavior (Figure 3E). For CF700 and CF1000, the impedance at 0.25 V exhibits a finite-space Warburg (FSW) response: a ~45° diffusion slope that transitions to a near-vertical rise as Li^+ transport becomes blocked at the carbon surface [67]. At 0 V, the response becomes less vertical, consistent with Li^+ penetrating into the carbon structure rather than being blocked at the surface.

CF1300 shows markedly different behavior. At 0.25 V, the Warburg feature flattens and curves upward toward higher impedance, indicating restricted or non-ideal Li^+ transport through a poorly passivating SEI. By 0 V, this feature sharpens into a more typical Warburg response, suggesting improved surface access but limited Li^+ penetration into the carbon structure. This behavior is consistent with continued SEI growth below 0.25 V and restricted pore accessibility, in agreement with the absence of a low-potential plateau in the voltage profile (Figure 2A).

EIS after three SEI formation cycles shows that CF1300 exhibits the highest interfacial resistance, while CF1000 has the lowest (Figure 3F). Titration results show CF1300 has the lowest total inorganic content (Table S4). In combination with the highest first-cycle irreversible capacity (Figure 2C), this indicates an extensive SEI rich in organics. The predominance of organics, which are generally less stable than inorganics, limits Li^+ conductivity and drives continued SEI growth, forming a thicker, less ionically conductive layer [14]. In contrast, CF1000 has the highest inorganic content (Table S4) and lowest first-cycle irreversible capacity (Figure 2C), consistent with a thin, inorganic-rich SEI that is both stable and ionically conductive. CF700 shows a higher first-cycle irreversible capacity than CF1000 despite forming less overall inorganic content (Table S4), indicating a more organic-rich layer that reduces stability and increases interfacial resistance. The high defect content and abundance of accessible ultra-micropores (Figure S4) provide numerous reactive sites, which could promote simultaneous electrolyte and salt decomposition, favoring organic SEI formation and limiting Li_2O/LiOH content (Figure 3C and Table S4).

Overall, CF1000 combines moderate defect density with a low fraction of ultra-micropores, providing a surface that efficiently passivates while limiting excessive organic SEI formation. The resulting SEI is thin, inorganic-rich and ionically conductive. SEI ionic conductivity governs the uniformity of Li deposition: an ionically conductive SEI enables homogeneous Li^+ transport, whereas a resistive SEI creates uneven, tortuous pathways that lead to localized ion accumulation.

4 | Carbon Fibers as Current Collectors for Lithium Metal Plating

Li nucleation during galvanostatic plating is identified by a voltage minimum, which occurs once Li ion storage sites within the carbon structure become saturated. The charge passed up to this voltage minimum corresponds to the pre-nucleation capacity. We define the nucleation overpotential (η_n) as the difference between the voltage minimum and the subsequent steady-state voltage plateau (Figure 4A), a metric reflecting both thermodynamic and kinetic barriers to nucleation [19, 68]. A strong inverse correlation between η_n and the pre-nucleation capacity was observed across all CF samples (Figure 4B). This correlation suggests that greater Li accommodation within the carbon structure lowers the effective nucleation barrier. CF1000, with a pre-nucleation capacity ~500 mA h g^{-1}, exhibits a shallow potential dip and low η_n (~0.02 V), outperforming Cu foil (~0.07 V) under the same conditions. In contrast, CF1300, with a pre-nucleation capacity < 150 mA h g^{-1}, shows a sharp potential drop and higher η_n (~0.07 V). The inverse correlation persisted over extended cycling, reinforcing the conclusion that enhanced Li accommodation within the carbon structure facilitates nucleation (Figure S12). The powder-derived electrode carbonized at 1000°C exhibits a higher η_n than all electrospun CFs (Figure S9), indicating that a continuous 3D fiber architecture is also essential for achieving low η_n, alongside sufficient pre-nucleation capacity.

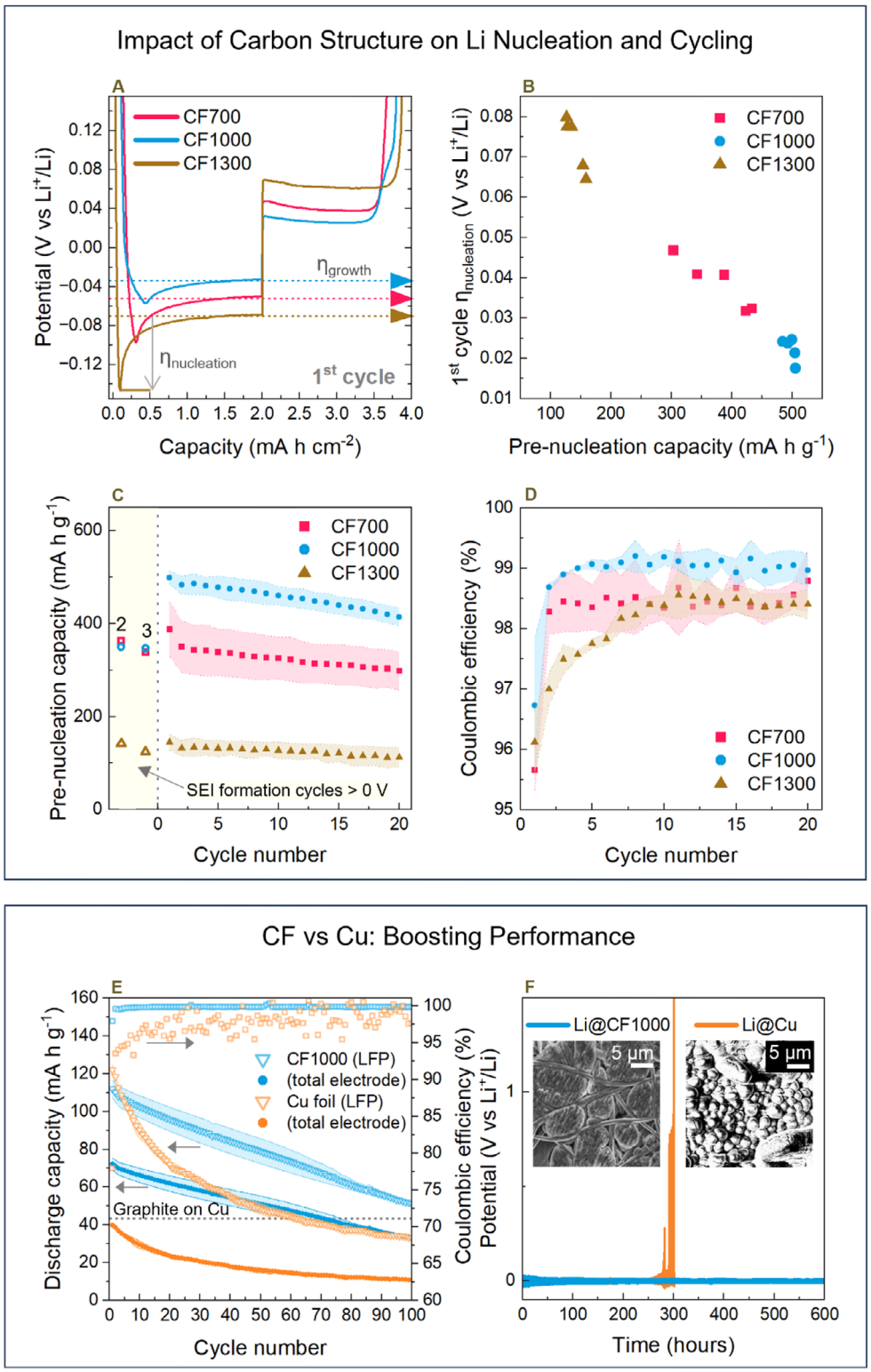

FIGURE 4 | Electrochemical characterization of Li metal plating. (A) Potential–capacity profiles of the first Li plating and stripping cycle at 1.0 mA cm^{-2} for CF700, CF1000, and CF1300. (B) First-cycle nucleation overpotential vs pre-nucleation capacity (capacity accumulated up to the voltage minimum) for five coin cells of CF700, CF1000, and CF1300. (C) Average pre-nucleation capacity vs cycle number; highlighted region shows reversible capacity above 0 V during the initial SEI formation cycles and the numbers refer to formation cycle number. (D) CE vs cycle number; data represents the average of five coin cells. (E) Discharge capacity and CE vs cycle number for zero-excess CF1000/LFP and Cu/LFP full cells cycled at C/5 charge and C/2 discharge (based on a total cathode active material capacity of 150 mA h g^{-1}), normalized to the LFP active mass or the total electrode mass; data represents the average of two coin cells; the theoretical discharge capacity normalized to the total electrode mass is included as a dashed line. (F) Potential vs time for Li@CF1000 and Li@Cu symmetric cells at 1.0 mA cm^{-2} with a (dis)charge capacity of 0.5 mA h cm^{-2}, with inset SEM images of the Li@CF1000 and Li@Cu electrodes prior to symmetric cell assembly.

To disentangle thermodynamic and kinetic effects on nucleation, we performed cyclic voltammetry (CV) at a slow scan rate of 0.1 mV s^{-1} with progressively extended negative cutoffs. Across all samples, nucleation initiated between −0.05 V and −0.06 V (Figure S13), suggesting similar thermodynamic nucleation barriers. The observed variation in nucleation during galvanostatic plating is therefore primarily attributed to kinetic factors, such as Li^+ transport and charge-transfer. CF1000 shows smaller increases in η_n with rising current density compared to CF700 and CF1300 (Figure S14), reflecting more favorable interfacial kinetics and, consequently, more uniform Li deposition and improved rate performance.

CF700 and CF1300 showed limited additional storage below 0 V prior to nucleation. In contrast, CF1000 exhibited notable storage capacity below 0 V, resulting in a large pre-nucleation capacity (Figure 4C). Similar hidden plateau-type capacities below 0 V have been previously reported for hard carbon anodes [56]. Pre-nucleation capacities in all samples remain relatively stable over 20 cycles, with only minor losses likely arising from irreversible Li^+ adsorption at strongly binding defect sites.

Pre-nucleation storage is governed by defect chemistry and local curvature, which together control Li^+ adsorption and early-stage cluster formation. Vacancy-type defects and vacancy complexes (V_C, N_CV_C, O_CV_C) contain unsaturated carbon (C) bonds or lone-pair-bearing-ad-atoms, strongly anchoring Li and stabilizing small clusters [41] (Figures S15 and S16). In contrast, substitutional dopants that preserve network connectivity (N_C, O_C) locally hinder Li binding but can stabilize neighboring sites, promoting lateral cluster growth (Figure S17). The amorphous, turbostratic carbon structure also creates local curvature and confinement. While small pores weaken Li-surface binding and increase Li–Li repulsion, destabilizing clusters, larger pores can reduce repulsion and better accommodate early-stage clusters [43, 44].

These structural factors explain the differences in pre-nucleation capacities across the CFs. CF700 has a high defect density, offering many reactive sites, but the dominance of sub-nanometer pores (<1 nm; Figure 1E) destabilizes Li clustering. CF1300 has larger pores, but its low density of vacancy-type defects limits the available sites for Li^+ adsorption and cluster nucleation. The absence of a pore-filling plateau in CF1300 may also reflect inaccessibility of the pores due to the formation of a thick, organic-rich SEI, as discussed previously. CF1000 exhibits a more favorable combination of moderate defect density and a substantial fraction of intermediate nanopores (~1.0–1.4 nm; Figure 1E), which are sufficiently large to accommodate and stabilize early-stage clusters while favoring both vacancy-type and N_c defects (Figure S8). This combination provides strong anchoring and promotes lateral cluster growth within the pores, leading to the highest pre-nucleation capacity among the CFs studied.

Following nucleation, the steady-state voltage reflects the Li growth overpotential (η_g), which is dominated by Li^+ mass transport from the bulk electrolyte through the SEI to the newly formed Li nuclei [68] (Figure 4A). CF1300 exhibits the highest η_g, followed by CF700, correlating well with the differences in SEI properties identified by XPS and EIS.

CF1000, which exhibits low nucleation and growth overpotentials, maintains an average CE of 99.0% over 200 cycles (Figures 4D and S18), demonstrating excellent cycling reversibility for a pristine CF [27, 30]. The lower nucleation and growth overpotentials of CF1000 promote more uniform Li deposition, limiting the formation of excessive reactive Li surface area and thereby slowing the progressive consumption of sacrificial $LiNO_3$ in the electrolyte. This not only slows gas evolution associated with $LiNO_3$ decomposition [69, 70], but also preserves nitrate-derived interphase components, contributing to sustained high CE and long cycle lifetimes. Furthermore, symmetric cells with Li-plated CF1000 electrodes demonstrate stable cycling over 3000 h with no short-circuiting, indicating effective dendrite suppression (Figure S19). In contrast, CF1300, which exhibits higher nucleation and growth overpotentials, exhibits highly unstable cycling behavior (Figures S18 and S19) and a lower average CE of 95.7% over the cycle lifetime.

To examine whether the behavior observed in half and symmetric cells translates to practical devices, full coin cells were assembled using CF700, CF1000, and CF1300 current collectors paired with a $LiFePO_4$ (LFP) cathode (Figure S20). Consistent with half-cell trends, CF1000 exhibits the highest first-cycle CE, the largest reversible pre-nucleation plateau capacity, and the lowest nucleation overpotential, demonstrating that its beneficial Li storage and nucleation behavior is preserved under full-cell conditions.

The CF1000/LFP full cell retains 64% of its initial capacity after 20 cycles and 53% over 50 cycles, compared with 48% and 32% for a Cu/LFP full cell (Figure 4E). While the Cu foil cell exhibits rapid active Li loss, CF1000 enables more stable cycling with gradual capacity decay. Similar trends are observed in symmetric cell tests, where Cu electrodes show a sharp overpotential increase after ~280 h, likely due to uneven, high-surface-area Li deposition and rapid active Li depletion (Figure 4F). Beyond electrochemical performance, CF current collectors offer substantial weight savings, with an areal density more than 20 times lower than Cu foil. Normalized to total electrode mass, CF1000 delivers more than three times the discharge capacity of Cu after 50 cycles and maintains capacities exceeding those of conventional LIBs over ~70 cycles.

5 | Mechanistic Understanding of Li Plating in Carbon Fibers

To investigate how pre-nucleation Li storage lowers the nucleation overpotential and enhances performance in CF1000, we employed ^{7}Li ssNMR spectroscopy, a powerful technique for distinguishing Li environments that has been widely used to study storage mechanisms in hard carbons [71, 72]. *Ex situ* spectra were collected at various cutoff points during cycling (Figure S21), while *operando* measurements were performed on a CF1000/Li half cell during one SEI formation cycle and six subsequent plating/stripping cycles (Figures 5A and S22).

The experimental spectra showed features in two distinct regions: a signal around 250 ppm arising from metallic Li (Li^0) [73], where Li atoms exist in a fully delocalized, metallic-bonding state and the resonance is shifted by the Knight effect (Figure 5B), and

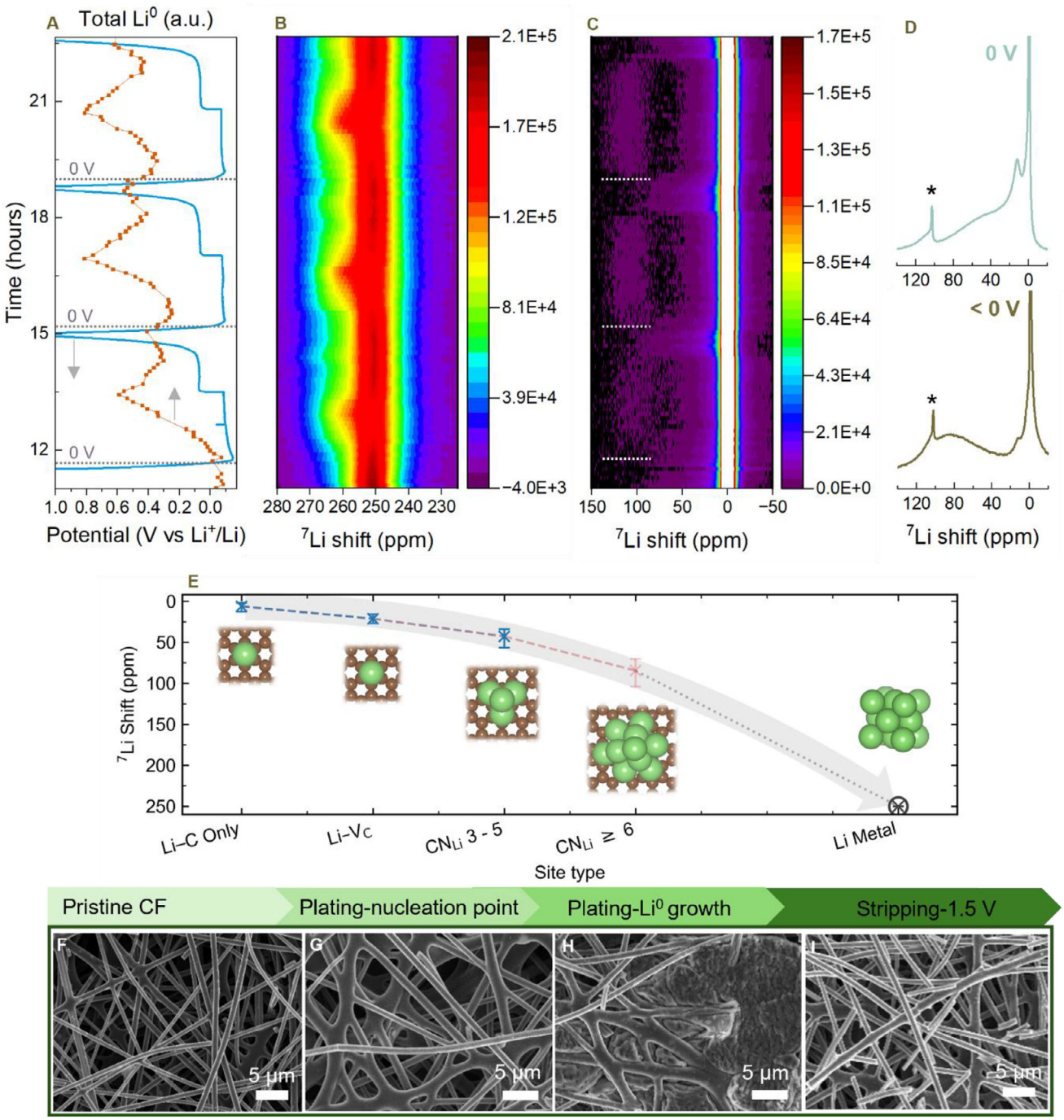

FIGURE 5 | ^{7}Li ssNMR characterization of Li nucleation and growth behavior. Voltage profile of CF1000 electrode and operando ^{7}Li ssNMR collected over three plating and stripping cycles. (A) Voltage profile (teal) and normalized total Li^0 intensity (bulk + plated Li; brown); the grey dotted lines show the times at which the potential is 0 V. *Operando* ^{7}Li ssNMR collected over the three plating and stripping cycles showing the (B) metallic and (C) diamagnetic regions; the white dotted lines show the times at which the potential is 0 V. (D) *Ex situ* NMR spectra at 0 V, and after 2 h of Li plating (<0 V); spinning sidebands are denoted with asterisks. (E) DFT simulated ^{7}Li shifts for different Li sites; the max-min markers show the 99% confidence intervals; the blue crosses represent no Li-states at the Fermi energy, the pink indicates Li-states at the Fermi energy, and the black corresponds to the metal reference taken from experiment. SEM images of (F) pristine CF1000, (G) *ex situ* CF1000 electrode cycled to −0.05 V, (H) *ex situ* CF1000 electrode after 2 h of plating, and (I) *ex situ* CF1000 electrode after the first plating/stripping cycle to 1.5 V.

a peak near 0 ppm corresponding to diamagnetic ^{7}Li in the electrolyte and SEI (Figure 5C). Within the region close to 0 ppm (the "diamagnetic" window), additional features correspond to partially reduced Li species associated with the carbon structure. At 0 V (dotted horizontal lines in Figure 5A,C), a broad ^{7}Li peak centered at ~50 ppm is present, as well as a sharp peak at ~12 ppm (Figure 5C,D). When the potential is below 0 V, the ~50 ppm component decreases, and a new broad feature emerges centered

at ~90–110 ppm (Figure 5C,D). This ~100 ppm feature does not appear during the SEI-formation cycle carried out entirely above 0 V (Figure S22), confirming that it is associated with processes specific to sub-0 V potentials.

To match these shifts with Li environments, DFT calculations were performed on Li atoms and Li clusters placed at representative sites identified in CF1000. For each configuration, the atomic charges were evaluated (Figure S23), and the ^{7}Li shifts were obtained (Figure 5E) from spin-polarized DFT calculations using the CP2K pNMR implementation, which evaluates orbital, Fermi-contact (FC), and dipolar hyperfine contributions within the Moon–Patchkovskii local moment formalism [74]. In this framework, the isotropic FC shift is directly proportional to the spin density at the Li nucleus, and for Li in these light element environments it is expected to dominate the paramagnetic contribution to the shift; orbital and pseudo-contact terms are estimated to be only a few ppm and are neglected in the discussion below. Quadrupolar interactions for ^{7}Li ($I = 3/2$) are not included in the computed shifts, but the associated second order quadrupolar offset of the central transition at the fields used experimentally is estimated to be well below 1 ppm. This offset is therefore negligible compared with the tens to hundreds of ppm shifts seen here.

For an isolated Li^+ ion bound to a graphene basal plane, the calculated ^{7}Li shift lies close to 0 ppm (4–12 ppm). This is consistent with a closed shell configuration in which the unpaired spin density at the Li nucleus is essentially zero and the FC term vanishes. Shifts in this range have been observed for Li^+ ions in hard carbons [71] and are also characteristic of the dilute stages of lithiated graphite, which remain electronically insulating [75]. In contrast, for small neutral Li clusters confined at the surface (Li- coordination number $CN_{Li} = 3–5$), the calculations predict a sizeable positive hyperfine shift that increases toward ≈ 50 ppm. In this regime, partially occupied Li-centered s-like cluster orbitals generate a finite unpaired spin density at the Li nuclei, producing a significant FC shift even though there is no extended conduction band [41]. The calculated shifts overlap with the experimental resonances of metallic dense intercalation stages in graphite (e.g., LiC_6/LiC_{12}), which appear at ~ +42–46 ppm [75]. In those graphitic compounds, however, the observed shift includes a metallic Knight shift (approximately 15% of that of Li metal), reflecting the presence of conduction electrons.

As the cluster size increases ($CN_{Li} \geq 6$, up to 12 Li atoms), the calculated isotropic shifts rise to ≈83 ppm. This trend reflects the growth of Li– connectivity and an increase in Li-centered spin density at the nuclei as the low energy cluster states become more metal-like [41]. However, these values remain well below the ^{7}Li Knight shift of bulk Li metal (~250 ppm) [76]. In the bulk, the Knight shift is itself a FC shift but scaled by the Pauli spin susceptibility of a continuous conduction band; in standard treatments it is proportional to the product of the FC hyperfine coupling and the electronic density of states at the Fermi level. In the confined clusters modeled here, the electronic states already display metallic characteristics, but the spectrum is still discrete, the effective low energy density of states and spin susceptibility are reduced relative to the bulk, and the resulting Knight-like FC shifts are correspondingly smaller. Moreover, within the CP2K pNMR implementation, the conversion from FC hyperfine couplings to shifts assumes a Curie–Weiss local moment susceptibility rather than an explicit Pauli susceptibility, so the computed cluster shifts should be viewed as local moment FC shifts approaching, but not fully realizing, the bulk Knight shift limit.

Within this framework, the experimental observation of a broad ^{7}Li resonance centered at ~100 ppm for potentials below 0 V vs Li/Li^+ (Figure 5C,D) is interpreted as arising from quasi-metallic Li domains. These domains are large enough to support metallic bonding and enhanced FC shifts but remain spatially confined within the carbon porosity so that the full bulk Knight shift is not recovered. The fact that the experimental shift (~100 ppm) lies between the calculated cluster values (~83 ppm) and the bulk metal value (~250 ppm) is consistent with such confined metallic behavior. Quantitative discrepancies at the level of a few tens of ppm are expected given the finite cluster sizes employed, the local moment susceptibility used in the pNMR formalism, the approximate treatment of orbital and pseudocontact terms, and the neglect of an explicit Pauli contribution to the spin susceptibility in the present DFT treatment.

The emergence of these larger, quasi-metallic clusters below 0 V also correlates with the additional pre-nucleation capacity observed experimentally before the nucleation point (Figure 4C). These quasi-metallic domains likely increase local electronic conductivity and create numerous, spatially distributed nucleation sites, helping to guide subsequent bulk metallic Li^0 deposition along the fiber surface and promote more uniform growth.

Detection of fully metallic Li^0 deposits is complicated by the dominant signal from the Li metal counter electrode. However, during cycling, the Li^0 signal increases in intensity and broadens toward higher chemical shifts from ~250 to 265 ppm. This change can be explained by two phenomena: the bulk magnetic susceptibility (BMS) and skin depth effects. The BMS shift is caused by local fields induced by the Li metal, which shows temperature independent paramagnetism and leads to different shifts between the bulk Li metal counter electrode and the metallic microstructures plated on CF1000. The skin depth effect alters the signal intensity, as the applied radio frequency only penetrates metallic Li^0 to a certain depth (~12 µm) and, therefore, the detected signal intensity is sensitive to the surface area and not the volume [77]. Since the diameter of the microstructures plated on CF1000 is smaller than the skin depth, the increase in Li^0 signal intensity should correlate directly with the mass of plated Li^0.

The normalized integral of the Li^0 peak (300–220 ppm) is plotted as "total Li^0" in Figure 5A. The sharp rise in this integral after extended discharge below 0 V in each cycle may correspond to the onset of Li^0 microstructure formation on the fiber surface, following the evolution of quasi-metallic domains [78, 79]. However, the true nucleation point may be partially obscured by concurrent stripping of Li^0 microstructures at the counter electrode. Because no Li^0 peak is detected in the *ex situ* sample discharged to −0.045 V (Figure S21), the quasi-metallic domains are likely to form prior to the appearance of quasi-metallic surface deposits. Further evidence for a multi-step deposition pathway is provided by scanning electron microscopy (SEM): immediately before the nucleation point (−0.05 V), no Li microstructures are

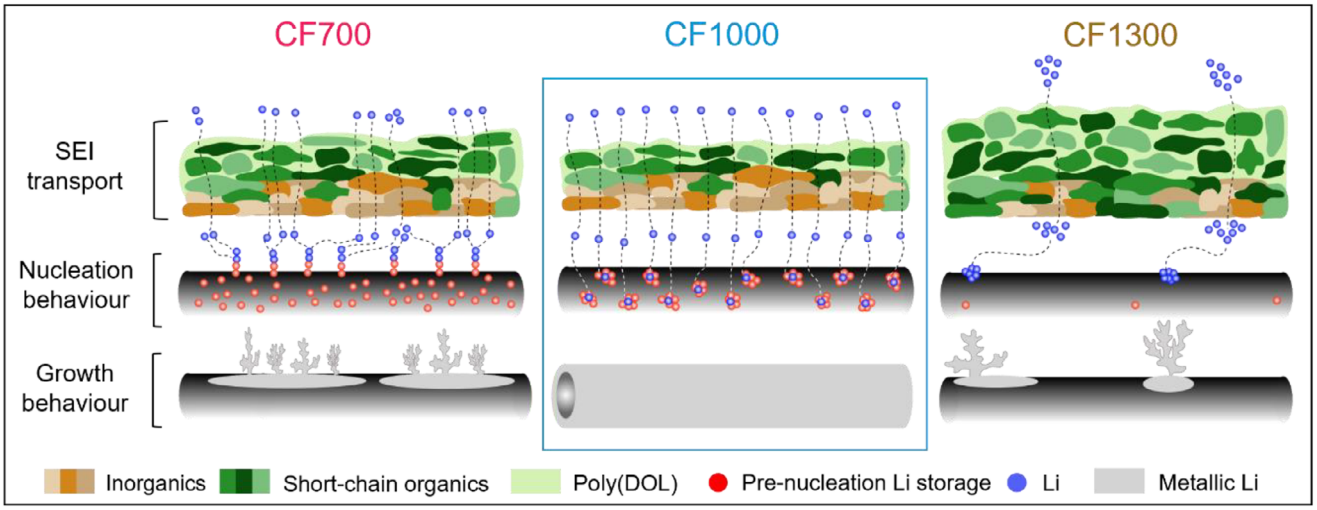

FIGURE 6 | Schematic diagram summarizing overall performance of CF700, CF1000, and CF1300.

visible. Instead, pronounced fiber swelling is observed, consistent with Li being accommodated internally (Figure 5F–H).

During each plating cycle, the total Li^0 signal increases as microstructures expand, and decreases during stripping as they are removed. Once surface Li^0 is fully stripped from CF1000, Li continues to redeposit on the counter electrode, causing a temporary rise in the total Li^0 signal. Simultaneously, the ~100 ppm feature vanishes, indicating the redistribution of Li stored within the pores and the reversion of domains to small clusters or adsorbed Li species (Figure 5I), which may subsequently act as nucleation sites in the next cycle (Figure 5C).

6 | Discussion

Figure 6 summarizes our results and highlights our proposed Li deposition mechanisms for each CF current collector, based on a combination of *ex situ* XPS analysis of SEI chemistry, direct spectroscopic evidence (^{7}Li NMR for CF1000), and comparative electrochemical and structural analysis.

CF1000 promotes the formation of a thin, ionically conductive and inorganic-rich SEI, enabling uniform Li^+ flux across the surface. A significant amount of Li is also stored within the CF's pore structure, where small, stabilized clusters evolve into confined metallic-like domains. These domains may provide locally enhanced electronic conductivity and numerous nucleation sites across the fiber surface, facilitating uniform Li plating, smooth deposition and improved reversibility.

In CF700, the SEI is more organic and less ionically conductive, which may lead to heterogeneous Li^+ flux. Its pore structure, dominated by micropores < 1 nm, restricts Li cluster growth and prevents the formation of metallic-like domains. Consequently, Li stored inside the carbon framework exists mainly as isolated adsorbed ions or small clusters (CN_{Li} = 3–5). At this size, the clusters do not exhibit metallic-like electronic characteristics and therefore cannot provide rapid electron-transfer pathways or act as effective nucleation centers. Nucleation is instead expected to occur predominantly at surface defect sites. These strongly binding sites concentrate Li^+ flux, promoting vertical Li growth rather than uniform deposition [32].

In CF1300, the thick, resistive, and predominantly organic SEI strongly hinders Li^+ transport, potentially leading to accumulation of ions at accessible surface regions. With minimal Li stored inside the carbon framework and reduced defect content, the number of energetically favorable nucleation sites is limited. As a result, Li deposition is uneven, resulting in high local current densities, the growth of high-surface-area metal structures, and poor reversibility [68, 78].

7 | Conclusion

In this work, we introduce a lignin-derived CF current collector to address both the sustainability and performance limitations of Cu foil and petrochemical-derived CF in ZELMBs. The exceptionally low density of the CFs makes them promising candidates in working toward high practical gravimetric energy densities. When paired against commercial LFP in a full cell, our CF current collector delivers superior cycling stability and achieves more than three times the discharge capacity of Cu foil after 50 cycles when normalized to the total electrode mass. In the future, further optimization of the full-cell system could be enabled by tuning of the electrolyte composition to understand the sacrificial nature of $LiNO_3$, its progressive reduction and generation of gaseous by-products, and these effects on long-term cycling performance.

Lignin-derived CFs inherently possess high defect content and abundant porosity, without the need for additional pore formers or heteroatom dopants, and these structural features can be precisely tuned through varying carbonization temperature. Our results show that the intrinsic defect chemistry and pore architecture of lignin-derived CFs govern SEI formation, Li nucleation behavior, and ultimately Li plating/stripping reversibility.

Surface defect density dictates SEI composition and passivation quality. Too few defects provide insufficient Li^+ binding and electron-rich sites, resulting in incomplete SEI formation

and continued electrolyte reduction at more negative potentials, producing a thick, resistive, organic-rich SEI. Too many defects introduce an excess of highly reactive sites, driving uncontrolled electrolyte decomposition and generating a mixed inorganic/organic SEI. A moderate defect density is optimal, enabling formation of a self-limiting, inorganic-rich SEI that supports homogeneous Li^+ transport.

Porosity plays an equally critical role in stabilizing Li prior to nucleation. Very small pores may destabilize Li clustering and prevent the development of metallic-like domains. In contrast, the intermediate nanopore regime observed for CF1000 provides both strong anchoring at vacancy-type defects and sufficient space to support the progression from adsorbed Li^+ to small clusters and ultimately metallic-like domains.

When an ionically conductive, inorganic-rich SEI is paired with a carbon framework capable of stabilizing metallic-like Li clusters, kinetic barriers to nucleation are substantially reduced across the surface. This synergy promotes spatially uniform Li nucleation and enables highly reversible Li plating/stripping.

Overall, this study demonstrates that rational control over the defect landscape and pore architecture of sustainable lignin-derived CFs provides a powerful strategy for tuning SEI chemistry and directing Li nucleation pathways. These insights establish clear design principles for high-performance, sustainable current collectors for next-generation ZELMBs.

8 | Experimental Section

8.1 | Materials

OSL extracted from beech wood was provided by the Fraunhofer Centre for Chemical-Biotechnological Processes (CBP) in Leuna. Poly(ethylene oxide) (PEO, M_W ~ 400,000 g mol^{-1}), sodium hydroxide (NaOH), and sodium carboxymethyl cellulose (M_W ~250,000 g mol^{-1}) were obtained from Sigma -Aldrich.

8.2 | Fabrication of Carbon Fiber Mats

The fabrication of CF mats followed procedures reported by our group [80]. Standard solutions were prepared by dissolving PEO (0.15 g) in aqueous NaOH (7.9 g, 0.5 M) for 3 h under magnetic stirring, followed by addition of OSL (1.05 g) and overnight stirring. The homogeneous solutions were transferred into a syringe (10 mL) with an 18-gauge needle and electrospun (Nanobox, Plaslab) at 25°C and 20% humidity, with a flow rate of 2 mL h^{-1}, 20 kV applied voltage, and 20 cm needle-to-collector distance. After spinning 6 mL, lignin mats (~100 µm thick) were removed, cut into strips, sandwiched between carbon felt, and heat-treated in an MTI 1200x tubular furnace under N_2. Carbonization was performed at 700, 1000, or 1300°C for 2 h with a 1°C min^{-1} heating rate, followed by furnace cooling under N_2. The mats were washed in DI water at 85°C for 2.5 h, rinsed with ethanol to remove salts and impurities, and dried overnight at 80°C under vacuum.

8.3 | Fabrication of Lignin-Derived Carbon Slurry Electrodes

Organosolv lignin (10 g) was carbonized in an STF furnace at 1000°C under N_2 (1°C min^{-1} ramp rate, 2 h dwell), then cooled to room temperature at 5°C min^{-1}. The resulting carbon was ground to a fine powder. Slurries containing 90 wt% carbonized lignin and 10 wt% sodium carboxymethyl cellulose binder were prepared in water and cast onto Cu metal foil using a 200 µm wet film thickness. Electrodes (11.12 mm diameter) were punched and dried overnight at 80°C under vacuum.

8.4 | Materials Characterization

2D (HSQC) NMR experiments were performed using a Bruker Advance III 400 MHz NMR spectrometer equipped with a 9.4 T magnet and a broadband PEG 5 mm probe at room temperature (25°C). For 2D (HSQC) spectroscopy, lignin (100 mg) was dissolved DMSO-d_6 (0.75 mL). NMR spectra were recorded using Bruker's "hsqcetgpsisp2.2" pulse program (adiabatic-pulse) with 1.5 s pulse delay. The number of transients was 64 and 256 time increments and were recorded in the ^{13}C dimension. The $^1J_{CH}$ used was 145 Hz. Data processing was performed using MestReNova. The central solvent peak was used as an internal reference (δ_c/δ_H 39.5/2.49 ppm). HSQC cross-signals were assigned by correlation with literature databases.

Small- and wide-angle X-ray scattering (SAXS/WAXS) measurements were performed on a Ganesha 300XL instrument (SAXSLAB) at 20°C under vacuum using a high-brilliance microfocus Cu Kα source (λ = 1.54 Å). The beam center and sample-to-detector distance were calibrated with a silver behenate standard (AgBeh). Pristine CF strips were sealed inside 1 mm borosilicate glass capillaries with hot glue. SAXS data were collected over q = 0.01–0.71 $Å^{-1}$ to probe nanoscale features, and WAXS data over q = 0.10–2.74 $Å^{-1}$ to analyze short-range order in scans of ~30 s each. Two-dimensional patterns were recorded using a Pilatus 300 K detector with a 2 mm beam stop and radially averaged using SAXSGUI software to obtain one-dimensional scattering profiles.

N_2 and carbon dioxide (CO_2) physisorption experiments were performed using a TriStar II PLUS analyzer (Micromeritics) at 77 K (N_2) and 273 K (CO_2), respectively. Prior to measurements, samples were degassed under vacuum at 200°C for 16 h using a Smart VacPrep system (Micromeritics) and Smart VacPrep software. Data evaluation was carried out using TriStar II PLUS software (version 3.00). For pore size distribution analysis, a heterogeneous surface two-dimensional non-local density functional theory (HS-2D-NLDFT) kernel for carbon with cylindrical pore geometry was applied to the adsorption branch of both CO_2 and N_2 isotherms. In addition, the Brunauer–Emmett–Teller (BET) method was applied to N_2 adsorption isotherms to calculate BET surface areas.

Raman spectroscopy was used to analyze the defect structures of carbon materials using a Senterra II Raman instrument with a laser wavelength of 532 nm. For each sample, spectra were collected from five different areas and averaged. The laser power was set to 2.5 mW with an integration time of 20 s to avoid sample heating or damage, and the spectral range of 50–4260 cm^{-1} was

recorded. See Supplementary Note 2 for details on the Raman fitting procedure.

XRD analysis was performed using a PANalytical X'Pert Pro diffractometer equipped with a Cu Kα source (λ = 1.5406 Å) operated at 40 kV and 15 mA. Powdered carbon samples were ground and loaded onto a flat sample holder to ensure a uniform surface. Diffraction patterns were collected in the 2θ range 10°–105° with a step size of 0.065° and a counting time of 445.5 s per step. The divergence slit was set to 0.229°, and the diffractometer radius was 145 mm. XRD patterns were analyzed and fitted using Gaussian functions to extract reflex positions and widths (see Supplementary Note 3 for details of the equations used).

XPS measurements were performed using a Thermo Fisher Nexsa spectrometer equipped with a monochromated Al Kα X-ray source (hν = 1486.6 eV). For electrochemical conditioning, half cells were discharged at a current density of 0.1 mA cm^{-2} using a LAND CT 3001A battery testing system to a lower potential limit of either 0.25 or 0 V. After cycling, coin cells were disassembled, and the electrodes were washed in excess dimethoxyethane (DME) for 5 min. Electrodes were then transferred to the XPS chamber using a Thermo Fisher vacuum transfer capsule to prevent air exposure and surface contamination. Depth profiling was carried out in situ by Ar^+ ion sputtering at 1000 eV for 5 s per cycle, with spectra acquired after each sputtering step. Data analysis and peak fitting were performed using Thermo Scientific Avantage software.

An SEM (Zeiss Auriga FIB-SEM) was used to characterize sample morphologies. For *ex situ* SEM analysis of cycled electrodes, half cells were discharged to different voltages at a current density of 1.0 mA cm^{-2} using a LAND CT 3001A battery testing system. After cycling, coin cells were disassembled, and the electrodes were washed in excess DME for 5 min. The electrodes were sealed in transfer tubes to minimize contamination or oxidation. All samples were mounted on stainless steel stubs using double-sided conductive carbon tape.

Operando ^{7}Li NMR experiments were performed on a Bruker Avance 300 MHz spectrometer (Larmor frequency for ^{7}Li being 116.6 MHz) using a solenoidal Ag-coated Cu coil. The spectra were acquired using a static automatic-tuning-and-matching probe (ATM VT X in situ WB NMR probe, NMR Service, eProbe). *Operando* ^{7}Li NMR was carried out using a custom PEEK in situ cell (NMR Service, eProbe) with CF1000 as the working electrode and Li metal as the counter electrode. The cell was precycled at 0.1 mA cm^{-2} between 0 and 1.5 V for one formation cycle, followed by six galvanostatic plating/stripping cycles at 1 mA cm^{-2} (discharge for 2 h; charge to 1.5 V). Spectra were acquired over the full ^{7}Li chemical shift range, alternating between two sets of acquisition parameters optimized for the diamagnetic and paramagnetic regions. For the diamagnetic region, spectra were acquired with a pulse width of 5 µs, recycle delay of 10 s, 16 scans, and an acquisition time of 0.066 s per spectrum. For the paramagnetic region, a pulse width of 6 µs, recycle delay of 1 s, 128 scans, and an acquisition time of 0.066 s per spectrum were used. This setup enabled continuous monitoring of Li evolution during cycling. Spectra were processed in Bruker TopSpin using automated phase and baseline correction and further analyzed in R, with integration of the Li metal peak (220–300 ppm) for quantification.

Ex situ solid-state ^{7}Li NMR measurements were performed on electrodes extracted from cells cycled to 0.2, 0, −0.045 V (just before nucleation) and after 2 h of plating. Cells were disassembled in an Ar-filled glovebox, and electrodes were dried for 2 h before being ground and mixed with pre-dried potassium bromide (KBr) (at 200°C for 40 h) to improve handling and reduce conductivity. The resulting powders were packed into 2.5 mm zirconia rotors for ^{7}Li solid-state NMR analysis. For the measurements a Bruker Avance III 500 MHz spectrometer (Larmor frequency for ^{7}Li being 194.4 MHz) equipped with a 2.5 mm H/FX MAS probe head (Bruker) was used. For each sample, two spectra at 20 kHz spinning were acquired with acquisition parameters optimized for either the diamagnetic or paramagnetic regions. For the diamagnetic region, spectra were acquired with a pulse width of 2.75 µs, recycle delay of 5 s, 1024 scans, and an acquisition time of 0.00655 s. For the paramagnetic region, spectra were acquired with a pulse width of 3.3 µs, recycle delay of 2 s, 8192 scans, and an acquisition time of 0.00416 s.

8.5 | Electrochemical Measurements

Electrochemical measurements were performed in stainless steel CR2032 coin cells (MTI Corporation) assembled in an Ar-filled glovebox (H_2O, O_2 < 0.5 ppm; mBraun) using a crimping machine (MTI Corporation). All cells, including half cells, symmetric cells, and full cells, contained 80 µL of 1 M lithium bis(trifluoromethanesulfonyl)imide (LiTFSI) in 1:1 (v/v) DOL/DME with 5 wt% $LiNO_3$ (CANRD) and a 16 mm separator comparable to Celgard 2400. Samples for *ex situ* SEM and XPS were disassembled from these coin cells at specified voltages.

8.6 | Half Cells

Li metal foil (0.12 mm, Goodfellow, 11.12 mm diameter) was used as both counter and reference electrode, with carbon fiber mats, carbon slurry electrodes or Cu metal foil (11.12 mm diameter) as the working electrode. Cu metal foil was sonicated with isopropanol twice for 5 min and dried at 80°C overnight under vacuum prior to cell assembly. SEI formation consisted of three discharge/charge cycles at 0.1 mA cm^{-2} between 1.5 and 0 V, followed by plating/stripping at 0.5–2.0 mA cm^{-2} with an areal capacity of 2.0 mA h cm^{-2}. Stripping was limited to 1.5 V, with instrument safety limits set between −5.0 and 5.0 V. Galvanostatic charge/discharge (GCD) profiles, differential capacity (dQ/dV) plots, and CE were recorded using a LAND CT 3001A battery tester. EIS was performed on a Bio-Logic VMP-300 potentiostat over 1 MHz to 0.01 Hz at selected potentials during the SEI formation protocol. CV was also carried out on the same instrument, with three scans between 0 and 1.5 V at 0.1 mV s^{-1}, followed by stepwise extension to more negative potentials (−0.01, −0.02, …, −0.10 V) with three scans at each range.

8.7 | Symmetric Cells

Li@CF and Li@Cu composite electrodes were prepared by depositing Li onto CF or Cu current collectors in a half cell configuration (1.0 mA cm^{-2} for 5 h). Cells were disassembled, electrodes rinsed with DME, dried, and reassembled in a symmetric cell configuration. Symmetric cells were cycled at 1.0 mA cm^{-2} for 0.5 h per (dis-)charge process using the LAND CT 3001A. The maximum and minimum potential limitations of the symmetric cells were set to be 5.0 and −5.0 V, respectively.

8.8 | Full Cells

Full cells were assembled using 11.12 mm diameter current collectors (carbon fiber mats or Cu metal foil) paired with 10 mm diameter $LiFePO_4$ (LFP) cathodes. Cells were cycled at C/10 for the first two charge/discharge cycles, followed by C/5 charge and C/2 discharge for subsequent cycles, based on a total cathode active material capacity of 150 mA h g^{-1}, where a rate of 1C corresponds to 1.58 mA cm^{-2}. Discharge capacities are reported both relative to the active cathode mass and relative to the total electrode mass, including the cathode coating, cathode current collector, and anode current collector. Cells were cycled between 3.0 and 3.8 V using a LAND CT 3001A battery tester.

8.9 | Computational Details

Defect formation energies for Li clustering on pristine and defective graphene (Nc, Oc, Vc, NcOc, NcVc, OcVc) were computed within the Zhang–Northrup [81] formalism, using both an isolated Li atom in vacuum and bulk Li metal as references to bracket the Li chemical-potential range. All DFT calculations were spin-polarized and performed at the Γ-point with CP2K [82] using the PBE [83, 84] exchange-correlation functional with D3(BJ) [85–88] dispersion, DZVP-SR-MOLOPT basis sets for the valence electrons and GTH pseudopotentials for the core electrons. ^{7}Li shifts (pNMR) were evaluated with the all-electron GAPW [89] linear-response implementation of Mondal et al. [74] in CP2K, employing an IGAIM gauge and pcS-2 [90] basis functions on Li, and converted to chemical shifts via a single reference shielding calibrated against solid lithium lactate; full computational details are provided in Supplementary Note 5.

Acknowledgements

The authors would like to thank the Fraunhofer Centre for Chemical-Biotechnological Processes for providing the lignin sample, and the Faraday Institution LiSTAR and degradation project grants FITG041, FIRG058, FIRG060, FIRG083, and FIRG082. H.A. thanks the Royal Society for funding through a University Research Fellowship URF\R1\231213. Part of this work was conducted at the Advanced Research Center for Nanolithography, a public-private partnership between the University of Amsterdam (UvA), Vrije Universiteit Amsterdam (VU), Rijksuniversiteit Groningen (RUG), the Netherlands Organization for Scientific Research (NWO), and the semiconductor equipment manufacturer ASML. This work made use of the Dutch national e-infrastructure with the support of the SURF Cooperative using Grant Number EINF-14923 and the authors thank SURF (www.surf.nl) for the support in using the National Supercomputer Snellius. E.O. is grateful for a WISE Fellowship from the NWO and acknowledge support via Holland High Tech through a public–private partnership in research and development within the Dutch top sector of High-Tech Systems and Materials (HTSM). C.D.M. thanks the EPSRC for funding via the doctoral prize fellowship scheme (postdoctoral pathways).

Conflicts of Interest

The authors declare no conflicts of interest.

Data Availability Statement

The data that support the findings of this study are available from the corresponding author upon reasonable request.

References

1. International Energy Agency (IEA). *The Role of Critical Minerals in Clean Energy Transitions*, (Paris 2021), https://www.iea.org/reports/the-role-of-critical-minerals-in-clean-energy-transitions.

2. Department for Business & Trade. *UK Battery Strategy*, (London 2023), https://www.gov.uk/government/publications/uk-battery-strategy.

3. A. J. Louli, A. Eldesoky, J. deGooyer, et al., "Different Positive Electrodes for Anode-Free Lithium Metal Cells," *Journal of the Electrochemical Society* 169, no. 4 (2022): 040517, https://doi.org/10.1149/1945-7111/ac62c4.

4. S. Nanda, A. Gupta, and A. Manthiram, "Anode-Free Full Cells: A Pathway to High-Energy Density Lithium-Metal Batteries," *Advanced Energy Materials* 11, no. 2 (2021): 1–18, https://doi.org/10.1002/aenm.202000804.

5. A. A. Assegie, J. H. Cheng, L. M. Kuo, W. N. Su, and B. J. Hwang, "Polyethylene Oxide Film Coating Enhances Lithium Cycling Efficiency of an Anode-Free Lithium-Metal Battery," *Nanoscale* 10, no. 13 (2018): 6125–6138, https://doi.org/10.1039/c7nr09058g.

6. X. Fan, L. Chen, O. Borodin, et al., "Non-Flammable Electrolyte Enables Li-Metal Batteries With Aggressive Cathode Chemistries," *Nature Nanotechnology* 13, no. 8 (2018): 715–722, https://doi.org/10.1038/s41565-018-0183-2.

7. T. T. Hagos, B. Thirumalraj, C. J. Huang, et al., "Locally Concentrated $LiPF_6$ in a Carbonate-Based Electrolyte With Fluoroethylene Carbonate as a Diluent for Anode-Free Lithium Metal Batteries," *ACS Applied Materials & Interfaces* 11, no. 10 (2019): 9955–9963, https://doi.org/10.1021/acsami.8b21052.

8. J. Alvarado, M. A. Schroeder, T. P. Pollard, et al., "Bisalt Ether Electrolytes: A Pathway towards Lithium Metal Batteries With Ni-Rich Cathodes," *Energy & Environmental Science* 12, no. 2 (2019): 780–794, https://doi.org/10.1039/c8ee02601g.

9. R. Weber, M. Genovese, A. J. Louli, et al., "Long Cycle Life and Dendrite-Free Lithium Morphology in Anode-Free Lithium Pouch Cells Enabled by a Dual-Salt Liquid Electrolyte," *Nature Energy* 4, no. 8 (2019): 683–689, https://doi.org/10.1038/s41560-019-0428-9.

10. J. Qian, B. D. Adams, J. Zheng, et al., "Anode-Free Rechargeable Lithium Metal Batteries," *Advanced Functional Materials* 26, no. 39 (2016): 7094–7102, https://doi.org/10.1002/adfm.201602353.

11. A. Pei, G. Zheng, F. Shi, Y. Li, and Y. Cui, "Nanoscale Nucleation and Growth of Electrodeposited Lithium Metal," *Nano Letters* 17, no. 2 (2017): 1132–1139, https://doi.org/10.1021/acs.nanolett.6b04755.

12. D. Lin, Y. Liu, and Y. Cui, "Reviving the Lithium Metal Anode for High-Energy Batteries," *Nature Nanotechnology* 12, no. 3 (2017): 194–206, https://doi.org/10.1038/nnano.2017.16.

13. C. Fang, J. Li, M. Zhang, et al., "Quantifying Inactive Lithium in Lithium Metal Batteries," *Nature* 572, no. 7770 (2019): 511–515, https://doi.org/10.1038/s41586-019-1481-z.

14. K. Tang, L. Tian, Y. Zhang, and Z. J. Xu, "Anode-Free Lithium Metal Batteries: A Promising Flexible Energy Storage System," *Journal*

of Materials Chemistry A 12, no. 27 (2024): 16268–16292, https://doi.org/10.1039/d4ta02003k.

15. E. Kim, W. Choi, S. Ryu, Y. Yun, S. Jo, and J. Yoo, "Effect of 3D Lithiophilic Current Collector for Anode-Free Li Ion Batteries," *Journal of Alloys and Compounds* 966 (2023): 171393, https://doi.org/10.1016/j.jallcom.2023.171393.

16. N. Li, T. Jia, Y. Liu, et al., "Super-Three-Dimensional Lithiophilic Cu-Based Current Collector for Anode-Free Lithium Metal Battery," *Materials Today Energy* 36 (2023): 101341, https://doi.org/10.1016/j.mtener.2023.101341.

17. V. Pande and V. Viswanathan, "Computational Screening of Current Collectors for Enabling Anode-Free Lithium Metal Batteries," *ACS Energy Letters* 4, no. 12 (2019): 2952–2959, https://doi.org/10.1021/acsenergylett.9b02306.

18. C. Sun, Y. Li, J. Jin, J. Yang, and Z. Wen, "ZnO Nanoarray-Modified Nickel Foam as a Lithiophilic Skeleton to Regulate Lithium Deposition for Lithium-Metal Batteries," *Journal of Materials Chemistry A* 7, no. 13 (2019): 7752–7759, https://doi.org/10.1039/C9TA00862D.

19. K. Yan, Z. Lu, H. W. Lee, et al., "Selective Deposition and Stable Encapsulation of Lithium Through Heterogeneous Seeded Growth," *Nature Energy* 1, no. 3 (2016): 16010, https://doi.org/10.1038/NENERGY.2016.10.

20. X. Han, H. Guo, B. Xing, et al., "A Facile Electrospinning Strategy to Prepare Cost-Effective Carbon Fibers as a Self-Supporting Anode for Lithium-Ion Batteries," *Fuel* 373 (2024): 132277, https://doi.org/10.1016/j.fuel.2024.132277.

21. Y. Zhao, J. Yan, J. Yu, and B. Ding, "Electrospun Nanofiber Electrodes for Lithium-Ion Batteries," *Macromolecular Rapid Communications* 44, no. 4 (2023): 2200740, https://doi.org/10.1002/marc.202200740.

22. S. H. Senthilkumar, B. Ramasubramanian, R. P. Rao, V. Chellappan, and S. Ramakrishna, "Advances in Electrospun Materials and Methods for Li-Ion Batteries," *Polymers* 15, no. 7 (2023): 1622, https://doi.org/10.3390/polym15071622.

23. S. Hong, S. Kim, M. Kim, et al., "Electrospun Carbon Nanofibers With Numerous Miniature Carbon Nanofibers for Free-Standing, Binder/Conductive Additive-Free Lithium-Ion Battery Anodes," *Energy & Environmental Materials* 8, no. 3 (2025): 12874, https://doi.org/10.1002/eem2.12874.

24. C. Yang, Y. Yao, S. He, H. Xie, E. Hitz, and L. Hu, "Ultrafine Silver Nanoparticles for Seeded Lithium Deposition Toward Stable Lithium Metal Anode," *Advanced Materials* 29, no. 38 (2017): 1702714, https://doi.org/10.1002/adma.201702714.

25. Y. Fang, S. L. Zhang, Z. P. Wu, D. Luan, and X. W. Lou, "A Highly Stable Lithium Metal Anode Enabled by Ag Nanoparticle–Embedded Nitrogen-Doped Carbon Macroporous Fibers," *Science Advances* 7, no. 21 (2021): abg3626, https://doi.org/10.1126/sciadv.abg3626.

26. Y. Fang, Y. Zeng, Q. Jin, et al., "Nitrogen-Doped Amorphous Zn–Carbon Multichannel Fibers for Stable Lithium Metal Anodes," *Angewandte Chemie International Edition* 60, no. 15 (2021): 8515–8520, https://doi.org/10.1002/anie.202100471.

27. J. Cui, S. Yao, M. Ihsan-Ul-Haq, J. Wu, and J. K. Kim, "Correlation Between Li Plating Behavior and Surface Characteristics of Carbon Matrix Toward Stable Li Metal Anodes," *Advanced Energy Materials* 9, no. 1 (2019): 1802777, https://doi.org/10.1002/aenm.201802777.

28. X. Chen, X. R. Chen, T. Z. Hou, et al., "Lithiophilicity Chemistry of Heteroatom-Doped Carbon to Guide Uniform Lithium Nucleation in Lithium Metal Anodes," *Science Advances* 5, no. 2 (2019): aau7728, https://doi.org/10.1126/sciadv.aau7728.

29. Y. Zhao, B. Chen, S. Xia, J. Yu, J. Yan, and B. Ding, "Selective Nucleation and Targeted Deposition Effect of Lithium in a Lithium-Metal Host Anode," *Journal of Materials Chemistry A* 9, no. 9 (2021): 5381–5389, https://doi.org/10.1039/d0ta11643b.

30. J. Xiang, L. Yuan, Y. Shen, et al., "Improved Rechargeability of Lithium Metal Anode via Controlling Lithium-Ion Flux," *Advanced Energy Materials* 8, no. 36 (2018): 1802352, https://doi.org/10.1002/aenm.201802352.

31. H. Kwon, J. H. Lee, Y. Roh, et al., "An Electron-Deficient Carbon Current Collector for Anode-Free Li-Metal Batteries," *Nature Communications* 12, no. 1 (2021): 5537, https://doi.org/10.1038/s41467-021-25848-1.

32. X. L. Zhang, L. Ma, Y. P. Cai, J. Fransaer, and Q. Zheng, "A Low-Fermi-Level Current Collector Enables Anode-Free Lithium Metal Batteries with Long Cycle Life," *Matter* 7, no. 2 (2024): 583–602, https://doi.org/10.1016/j.matt.2023.11.017.

33. S. Hérou, M. Crespo Ribadeneyra, P. Schlee, et al., "The Impact of Having an Oxygen-Rich Microporous Surface in Carbon Electrodes for High-Power Aqueous Supercapacitors," *Journal of Energy Chemistry* 53 (2020): 36–48, https://doi.org/10.1016/j.jechem.2020.04.068.

34. M. Baloch and J. L. B. Labidi, "Lignin Biopolymer: The Material of Choice for Advanced Lithium-Based Batteries," *RSC Advances* 11, no. 38 (2021): 23644–23653, https://doi.org/10.1039/d1ra02611a.

35. J. Zhang, H. Xiang, Z. Cao, S. Wang, and M. Zhu, "Research Progress of Lignin-Derived Materials in Lithium/Sodium Ion Batteries," *Green Energy and Environment* 10, no. 2 (2025): 322–344, https://doi.org/10.1016/j.gee.2024.05.001.

36. Z. Xu, Z. Guo, R. Madhu, et al., "Homogenous Metallic Deposition Regulated by Defect-Rich Skeletons for Sodium Metal Batteries," *Energy & Environmental Science* 14, no. 12 (2021): 6381–6393, https://doi.org/10.1039/d1ee01346g.

37. M. J. Suota, T. A. da Silva, S. F. Zawadzki, et al., "Chemical and Structural Characterization of Hardwood and Softwood LignoForce™ Lignins," *Industrial Crops and Products* 173 (2021): 114138, https://doi.org/10.1016/j.indcrop.2021.114138.

38. S. Hérou, M. Crespo, and M. Titirici, "Investigating the Effects of Activating Agent Morphology on the Porosity and Related Capacitance of Nanoporous Carbons," *CrystEngComm* 22, no. 9 (2020): 1560–1567, https://doi.org/10.1039/c9ce01702j.

39. H. Au, H. Alptekin, A. C. S. Jensen, et al., "A Revised Mechanistic Model for Sodium Insertion in Hard Carbons," *Energy & Environmental Science* 13, no. 10 (2020): 3469–3479, https://doi.org/10.1039/d0ee01363c.

40. A. C. Ferrari and J. Robertson, "Interpretation of Raman Spectra of Disordered and Amorphous Carbon," *Physical Review B* 61, no. 20 (2000): 14095–14107, https://doi.org/10.1103/PhysRevB.61.14095.

41. J. Cottom, Q. Cai, and E. Olsson, "Vacancy Enhanced Li, Na, and K Clustering on Graphene," *Sustainable Energy Fuels* 9, no. 10 (2025): 2813–2826, https://doi.org/10.1039/d5se00130g.

42. E. Olsson, J. Cottom, H. Alptekin, et al., "Investigating the Role of Surface Roughness and Defects on EC Breakdown, as a Precursor to SEI Formation in Hard Carbon Sodium-Ion Battery Anodes," *Small* 18, no. 43 (2022): 2200177, https://doi.org/10.1002/smll.202200177.

43. E. Olsson, J. Cottom, H. Au, et al., "Elucidating the Effect of Planar Graphitic Layers and Cylindrical Pores on the Storage and Diffusion of Li, Na, and K in Carbon Materials," *Advanced Functional Materials* 30 (2020), https://doi.org/10.1002/adfm.201908209.

44. E. Olsson, J. Cottom, and Q. Cai, "Defects in Hard Carbon: Where Are They Located and How Does the Location Affect Alkaline Metal Storage?," *Small* 17, no. 18 (2021): 2007652, https://doi.org/10.1002/smll.202007652.

45. E. Olsson, G. Chai, M. Dove, and Q. Cai, "Adsorption and Migration of Alkali Metals (Li, Na, and K) on Pristine and Defective Graphene Surfaces," *Nanoscale* 11, no. 12 (2019): 5274–5284, https://doi.org/10.1039/c8nr10383f.

46. H. Adenusi, G. A. Chass, S. Passerini, K. V. Tian, and G. Chen, "Lithium Batteries and the Solid Electrolyte Interphase (SEI)—Progress

and Outlook," *Advanced Energy Materials* 13, no. 10 (2023): 2203307, https://doi.org/10.1002/aenm.202203307.

47. D. Aurbach, "Review of Selected Electrode–Solution Interactions Which Determine the Performance of Li and Li Ion Batteries," *Journal of Power Sources* 89 (2000): 206–218, https://doi.org/10.1016/S0378-7753(00)00431-6.

48. D. Aurbach, O. Youngman, Y. Gofer, and A. Meitav, "The Electrochemical Behaviour of 1,3-Dioxolane—$LiClO_4$ Solutions—I. Uncontaminated Solutions," *Electrochimica Acta* 35, no. 3 (1990): 625–638, https://doi.org/10.1016/0013-4686(90)87055-7.

49. Y. Chen, T. Wang, H. Tian, D. Su, Q. Zhang, and G. Wang, "Advances in Lithium–Sulfur Batteries: From Academic Research to Commercial Viability," *Advanced Materials* 33, no. 29 (2021): 2003666, https://doi.org/10.1002/adma.202003666.

50. G. M. Hobold, J. Lopez, R. Guo, et al., "Moving Beyond 99.9% Coulombic Efficiency for Lithium Anodes in Liquid Electrolytes," *Nature Energy* 6, no. 10 (2021): 951–960, https://doi.org/10.1038/s41560-021-00910-w.

51. Y. Liu, D. Lin, Y. Li, et al., "Solubility-Mediated Sustained Release Enabling Nitrate Additive in Carbonate Electrolytes for Stable Lithium Metal Anode," *Nature Communications* 9, no. 1 (2018): 3656, https://doi.org/10.1038/s41467-018-06077-5.

52. J. Zheng, J. Wang, T. Guo, et al., "Highly Thermostable Interphase Enables Boosting High-Temperature Lifespan for Metallic Lithium Batteries," *Small* 19, no. 15 (2023): 2207742, https://doi.org/10.1002/smll.202207742.

53. S. Stuckenberg, M. M. Bela, C. T. Lechtenfeld, et al., "Influence of $LiNO_3$ on the Lithium Metal Deposition Behavior in Carbonate-Based Liquid Electrolytes and on the Electrochemical Performance in Zero-Excess Lithium Metal Batteries," *Small* 20, no. 6 (2024): 2305203, https://doi.org/10.1002/smll.202305203.

54. T. Jaumann, J. Balach, M. Klose, S. Oswald, J. Eckert, and L. Giebeler, "Role of 1,3-Dioxolane and $LiNO_3$ Addition on the Long Term Stability of Nanostructured Silicon/Carbon Anodes for Rechargeable Lithium Batteries," *Journal of The Electrochemical Society* 163, no. 3 (2016): A557–A564, https://doi.org/10.1149/2.1011603jes.

55. Y. Sun, H. W. Lee, Z. W. Seh, et al., "High-Capacity Battery Cathode Prelithiation to Offset Initial Lithium Loss," *Nature Energy* 1, no. 1 (2016): 15008, https://doi.org/10.1038/nenergy.2015.8.

56. Y. Li, A. Vasileiadis, Q. Zhou, et al., "Origin of Fast Charging in Hard Carbon Anodes," *Nature Energy* 9, no. 2 (2024): 134–142, https://doi.org/10.1038/s41560-023-01414-5.

57. K. Ciosek Högström, S. Malmgren, M. Hahlin, et al., "The Buried Carbon/Solid Electrolyte Interphase in Li-Ion Batteries Studied by Hard X-Ray Photoelectron Spectroscopy," *Electrochimica Acta* 138 (2014): 430–436, https://doi.org/10.1016/j.electacta.2014.06.129.

58. A. J. Slate, D. A. C. Brownson, A. S. Abo Dena, G. C. Smith, K. A. Whitehead, and C. E. Banks, "Exploring the Electrochemical Performance of Graphite and Graphene Paste Electrodes Composed of Varying Lateral Flake Sizes," *Physical Chemistry Chemical Physics* 20, no. 30 (2018): 20010–20022, https://doi.org/10.1039/c8cp02196a.

59. P. Verma, P. Maire, and P. Novák, "A Review of the Features and Analyses of the Solid Electrolyte Interphase in Li-Ion Batteries," *Electrochimica Acta* 55, no. 22 (2010): 6332–6341, https://doi.org/10.1016/j.electacta.2010.05.072.

60. C. K. Chan, R. Ruffo, S. S. Hong, and Y. Cui, "Surface Chemistry and Morphology of the Solid Electrolyte Interphase on Silicon Nanowire Lithium-Ion Battery Anodes," *Journal of Power Sources* 189, no. 2 (2009): 1132–1140, https://doi.org/10.1016/j.jpowsour.2009.01.007.

61. E. Peled and S. Menkin, "Review—SEI: Past, Present and Future," *Journal of The Electrochemical Society* 164, no. 7 (2017): A1703–A1719, https://doi.org/10.1149/2.1441707jes.

62. G. M. Hobold, C. Wang, K. Steinberg, Y. Li, and B. M. Gallant, "High Lithium Oxide Prevalence in the Lithium Solid–Electrolyte Interphase for High Coulombic Efficiency," *Nature Energy* 9, no. 5 (2024): 580–591, https://doi.org/10.1038/s41560-024-01494-x.

63. W. Li, H. Yao, K. Yan, et al., "The Synergetic Effect of Lithium Polysulfide and Lithium Nitrate to Prevent Lithium Dendrite Growth," *Nature Communications* 6 (2015): 7436, https://doi.org/10.1038/ncomms8436.

64. Y. Mao, T. Wang, F. Yin, and C. I. Sun, "In Situ Formation of Li_3N Interlayer Enhancing Interfacial Stability of Solid-State Lithium Batteries," *Journal of Colloid and Interface Science* 685 (2025): 595–603, https://doi.org/10.1016/j.jcis.2025.01.151.

65. S. J. An, J. Li, C. Daniel, D. Mohanty, S. Nagpure, and D. L. Wood, "The State of Understanding of the Lithium-Ion-Battery Graphite Solid Electrolyte Interphase (SEI) and Its Relationship to Formation Cycling," *Carbon* 105 (2016): 52–76, https://doi.org/10.1016/j.carbon.2016.04.008.

66. Q. Lv, N. Wang, W. Si, et al., "Pyridinic Nitrogen Exclusively Doped Carbon Materials as Efficient Oxygen Reduction Electrocatalysts for Zn-Air Batteries," *Applied Catalysis B: Environmental* 261 (2020): 118234, https://doi.org/10.1016/j.apcatb.2019.118234.

67. M. Oldenburger, B. Bedürftig, A. Gruhle, et al., "Investigation of the Low Frequency Warburg Impedance of Li-Ion Cells by Frequency Domain Measurements," *Journal of Energy Storage* 21 (2019): 272–280, https://doi.org/10.1016/j.est.2018.11.029.

68. P. Biswal, S. Stalin, A. Kludze, S. Choudhury, and L. A. Archer, "Nucleation and Early Stage Growth of Li Electrodeposits," *Nano Letters* 19, no. 11 (2019): 8191–8200, https://doi.org/10.1021/acs.nanolett.9b03548.

69. A. Jozwiuk, B. B. Berkes, T. Weiß, H. Sommer, J. Janek, and T. Brezesinski, "The Critical Role of Lithium Nitrate in the Gas Evolution of Lithium–Sulfur Batteries," *Energy & Environmental Science* 9, no. 8 (2016): 2603–2608, https://doi.org/10.1039/c6ee00789a.

70. M. Graf, L. Reuter, S. Qian, et al., "Understanding the Effect of Lithium Nitrate as Additive in Carbonate-Based Electrolytes for Silicon Anodes," *Journal of The Electrochemical Society* 171, no. 9 (2024): 090514, https://doi.org/10.1149/1945-7111/ad71f7.

71. F. Chevallier, M. Letellier, M. Morcrette, et al., "In Situ 7Li-Nuclear Magnetic Resonance Observation of Reversible Lithium Insertion Into Disordered Carbons," *Electrochemical and Solid-State Letters* 6, no. 11 (2003): A225–A228, https://doi.org/10.1149/1.1612011.

72. M. Letellier, F. Chevallier, F. Béguin, E. Frackowiak, and J. N. Rouzaud, "The First in Situ 7Li NMR Study of the Reversible Lithium Insertion Mechanism in Disorganised Carbons," *Journal of Physics and Chemistry of Solids* 65, no. 2–3 (2004): 245–251, https://doi.org/10.1016/j.jpcs.2003.10.022.

73. A. B. Gunnarsdóttir, C. V. Amanchukwu, S. Menkin, and C. P. Grey, "Noninvasive In Situ NMR Study of 'Dead Lithium' Formation and Lithium Corrosion in Full-Cell Lithium Metal Batteries," *Journal of the American Chemical Society* 142, no. 49 (2020): 20814–20827, https://doi.org/10.1021/jacs.0c10258.

74. F. Balzaretti and J. Voss, "Density Functional Tight-Binding Models for Band Structures of Transition-Metal Alloys and Surfaces Across the D-Block," *Journal of Chemical Theory and Computation* 20 (2024): 7272, https://doi.org/10.1021/acs.jctc.4c00345.

75. D. C. Maxwell, C. A. O'Keefe, C. Xu, and C. P. Grey, "C 13 NMR Study of the Electronic Structure of Lithiated Graphite," *Physical Review Materials* 7, no. 6 (2023): 065402, https://doi.org/10.1103/PhysRevMaterials.7.065402.

76. V. Küpers, M. Kolek, P. Bieker, M. Winter, and G. Brunklaus, "In Situ 7Li-NMR Analysis of Lithium Metal Surface Deposits With Varying Electrolyte Compositions and Concentrations," *Physical Chemistry Chemical Physics* 21, no. 47 (2019): 26084–26094, https://doi.org/10.1039/c9cp05334d.

77. A. B. Gunnarsdóttir, S. Vema, S. Menkin, L. E. Marbella, and C. P. Grey, "Investigating the Effect of a Fluoroethylene Carbonate Additive on Lithium Deposition and the Solid Electrolyte Interphase in Lithium Metal Batteries using in situ NMR Spectroscopy," *Journal of Materials Chemistry A Mater* 8, no. 30 (2020): 14975–14992, https://doi.org/10.1039/d0ta05652a.

78. X. Su, F. Dogan, J. Ilavsky, V. A. Maroni, D. J. Gosztola, and W. Lu, "Mechanisms for Lithium Nucleation and Dendrite Growth in Selected Carbon Allotropes," *Chemistry of Materials* 29, no. 15 (2017): 6205–6213, https://doi.org/10.1021/acs.chemmater.7b00072.

79. K. Gotoh, T. Yamakami, I. Nishimura, et al., "Mechanisms for Overcharging of Carbon Electrodes in Lithium-ion/sodium-ion Batteries Analysed by Operando solid-state NMR," *Journal of Materials Chemistry A* 8, no. 29 (2020): 14472–14481, https://doi.org/10.1039/d0ta04005c.

80. S. Hérou, J. J. Bailey, M. Kok, et al., "High-Density Lignin-Derived Carbon Nanofiber Supercapacitors With Enhanced Volumetric Energy Density," *Advanced Science* 8, no. 17 (2021): 2100016, https://doi.org/10.1002/advs.202100016.

81. S. B. Zhang and J. E. Northrup, "Chemical Potential Dependence of Defect Formation Energies in GaAs: Application to Ga Self-Diffusion," *Physical Review Letters* 67 (1991): 17.

82. T. D. Kühne, M. Iannuzzi, M. Del Ben, et al., "CP2K: An Electronic Structure and Molecular Dynamics Software Package -Quickstep: Efficient and Accurate Electronic Structure Calculations," *The Journal of Chemical Physics* 152, no. 19 (2020): 194103, https://doi.org/10.1063/5.0007045.

83. J. P. Perdew, K. Burke, and M. Ernzerhof, "Generalized Gradient Approximation Made Simple," *Physical Review Letters* 77 (1996): 3865–3868, https://doi.org/10.1103/PhysRevLett.77.3865.

84. J. P. Perdew, K. Burke, and M. Ernzerhof, "Generalized Gradient Approximation Made Simple [Phys. Rev. Lett. 77, 3865 (1996)]," *Physical Review Letters* 78 (1997): 1396, https://doi.org/10.1103/PhysRevLett.78.1396.

85. E. R. Johnson and A. D. Becke, "A Post-Hartree-Fock Model of Intermolecular Interactions: Inclusion of Higher-Order Corrections," *The Journal of Chemical Physics* 124, no. 17 (2006): 174104, https://doi.org/10.1063/1.2190220.

86. S. Grimme, S. Ehrlich, and L. Goerigk, "Effect of the Damping Function in Dispersion Corrected Density Functional Theory," *Journal of Computational Chemistry* 32, no. 7 (2011): 1456–1465, https://doi.org/10.1002/jcc.21759.

87. S. Grimme, J. Antony, S. Ehrlich, and H. Krieg, "A Consistent and Accurate Ab Initio Parametrization of Density Functional Dispersion Correction (DFT-D) for the 94 Elements H-Pu," *The Journal of Chemical Physics* 132, no. 15 (2010): 154104, https://doi.org/10.1063/1.3382344.

88. S. Grimme, J. Antony, T. Schwabe, and C. Mück-Lichtenfeld, "Density Functional Theory With Dispersion Corrections for Supramolecular Structures, Aggregates, and Complexes of (Bio)Organic Molecules," *Organic & Biomolecular Chemistry* 5, no. 5 (2007): 741–758, https://doi.org/10.1039/b615319b.

89. G. Lippert, J. Hutter, and M. Parrinello, "The Gaussian and Augmented-Plane-Wave Density Functional Method for Ab Initio Molecular Dynamics Simulations," *Theoretical Chemistry Accounts: Theory, Computation, and Modeling (Theoretica Chimica Acta)* 103 (1999): 124–140, https://doi.org/10.1007/s002140050523.

90. F. Jensen, "Basis Set Convergence of Nuclear Magnetic Shielding Constants Calculated by Density Functional Methods," *Journal of Chemical Theory and Computation* 4, no. 5 (2008): 719–727, https://doi.org/10.1021/ct800013z.

Supporting Information

Additional supporting information can be found online in the Supporting Information section.

Supporting File 1: aenm70857-sup-0001-SuppMat.docx.